University of Crete

Department of Material Science and Technology

Novel optical breadboard beam steering techniques for space applications

Thesis submitted in partial fulfillment of the requirements for the Master of Science

Konstantinos Mavrakis

Supervising Committee

Dimitris G. Papazoglou

Assistant Professor, Department of Materials Science and Technology, UoC

Wolf von Klitzing

Cretan Matter Waves research group leader, IESL-FORTH

George Kopidakis

Associate Professor, Department of Materials Science and Technology, UoC

Abstract

Beam steering is a critical issue in optical space applications. The technical requirements with respect to the angular and translational beam alignment and the optical path length are at the limits of current mounting and optical component fabrication technology. Furthermore, stability is of paramount importance, since long and short term fluctuations in temperature as well as shocks and vibrations during space missions can dramatically affect the performance of the optical components and of the whole system.

This work focuses on experimentally demonstrating novel techniques, using passive optical components, which allow precise beam-steering on an optical breadboard. The passive optical components are inserted to the system to compensate for inaccuracies during manufacturing stages of the components. Therefore, the manufactured components do not need to be flawless so the manufacturing tolerances are relaxed thus reducing the required technologies. Moreover, these techniques are less sensitive to misalignments and lead to reduced precision requirements by the optical components. Lastly, the stability of these techniques is also tested on prototype optical breadboards.

Περίληψη

Η ευθυγράμμιση δεσμών λέιζερ είναι καθοριστικός παράγοντας στις εφαρμογές των διαστημικών αποστολών. Οι τεχνικές προδιαγραφές σχετικά με την ακρίβεια της τοποθέτησης των υποσυστημάτων, τον οπτικό δρόμο και την ευθυγράμμιση της δέσμης είναι στα όρια των σύγχρονων τεχνολογιών τοποθέτησης και κατασκευής οπτικών. Επιπλέον, η σταθερότητα του συστήματος είναι σημαντικός παράγοντας καθώς βραχυχρόνιες και μακρυχρόνιες διακυμάνσεις στην θερμοκρασία αλλά και δονήσεις κατά την διάρκεια μίας διαστημικής αποστολής μπορούν να επηρεάσουν δραματικά την απόδοση των οπτικών αλλά και συνολικά του συστήματος.

Στα πλαίσια αυτής της διπλωματικής εργασίας εστιάσαμε στην πειραματική εφαρμογή καινοτόμων μεθόδων, χρησιμοποιώντας παθητικά οπτικά υποσυστήματα τα οποία επιτρέπουν ακριβή ευθυγράμμιση της δέσμης σε μία οπτική διάταξη. Τα παθητικά οπτικά υπεισέρχονται στο σύστημα ώστε να αντισταθμίσουν για τυχόν αστοχίες κατά την διάρκεια των κατασκευαστικών σταδίων. Συνεπώς, τα κατασκευασμένα στοιχεία δεν απαιτείται να είναι αψεγάδιαστα και κατά συνέπεια οι κατασκευαστικές ανοχές αμβλύνονται και οι απαιτούμενες τεχνολογίες μειώνονται. Επιπρόσθετα, αυτές οι τεχνικές είναι λιγότερο ευαίσθητες σε απευθυγραμμίσεις και οδηγούν σε μείωση της απαιτούμενης ακρίβειας των οπτικών στοιχείων. Τέλος, η οπτική σταθερότητα των χρησιμοποιούμενων τεχνικών εξετάζεται σε πρότυπες οπτικές διατάξεις.

Preface

This MSc project was part of a research program which was financially supported by the European Space Agency (ESA). Therefore, some details are protected by copyright law and were not mentioned intentionally.

The research program of the European Space Agency (ESA) was titled “Optical Breadboard Technologies for Complex Space Missions” project and took place in the facilities of the Institute of Electronic Structure and Laser (IESL) at the Foundation of Research and Technology - Hellas (FORTH) under the supervision of Professor Dimitris Papazoglou, Dr Wolf von Klitzing (Researcher, IESL-FORTH) and Professor George Kopidakis.

Acknowledgements

I would like to thank my supervisor Prof. Dimitris Papazoglou for his invaluable guidance he has provided me throughout the duration of this project. I am grateful for the time he spent on transmitting knowledge and experience to me. His guidance and criticism were at all times instructive and beneficial.

I would also like to express my gratitude towards Dr. Wolf von Klitzing for introducing me to an innovative research group and presenting to me the opportunity to work on a unique research project. Participating to the materialization of this concept was an extremely learning and mind changing experience for me. From the very early steps of testing the simple ideas to assembling the final breadboard, the whole process was edifying and intriguing.

Furthermore, I should also thank deeply Dr Konstantinos Poulios for aiding and providing valuable comments on this thesis. His persistence on doing everything properly throughout the project was really unique and exemplary.

I could not avoid mentioning Giannis Drougkakis. His master thesis and theoretical analysis were the foundation for this project. Working together every day to assemble a prototype breadboard was truly an unprecedented process. Thank you for everything.

Every member of Bose-Enstein Condesation lab had its own contribution and I feel gratitude towards them. From Vasiliki Bolpasi and George Vasilakis to Hector Mass, Saurabh Pandey and Mikis Milonakis, they all have their fair share of contribution.

Finally, I would like to thank my family for their unending support and encouragement. I also owe a distinct mention to Konstantina Sfakianaki for her support and help. My gratitude is immense.

Table of Contents

Acronyms

Acronym	Explanation
AR	Anti-Reflection
CAD	Computer Assisted Drawing
CCD	Charge Coupled Device
CE	Coupling Efficiency
CTE	Coefficient of Thermal Expansion
DBR	Distributed Bragg Reflectors
DDR	Detailed Design Review
DFB	Distributed Feedback
FP	Fabry-Perot
GI	Graded index
IR	Infrared Radiation
LED	Light Emitting Diode
MCVD	Modified chemical vapor deposition
MM	Multimode
MQW	Multiple Quantum Wells
NA	Numerical Aperture
NOA	Norland Optical Adhesive
OBST	Optical Beam Steering Technology
PBS	Polarizing Beam Splitter
PEEK	Polyether ether ketone
PM	Polarization Maintaining
QW	Quantum Well
RMS	Root Mean Square
SI	Step index
SM	Singlemode
Tg	Glass Transition Temperature
UV	Ultra Violet
VCSEL	Vertical Cavity Surface Emitting Laser

1. Introduction

The aim of the project is to design and experimentally implement a novel approach to beam steering techniques. This approach is mainly applied to schemes where high and robust power transmission between Single Mode (SM) optical fibers is the main concern, such as cold atom experiments in space where laser beam traverse a number of passive and active optical elements and couple into SM fibers. Even in simple optical set ups and breadboards (with the simplest one being a transmitting optical fiber with a collimating lens, free space propagation and a receiving optical fiber with a lens, Figure 1.1) achieving high power transmission is not trivial and requires high accuracy.

Figure 1.1 Simple breadboard consisting of a transmitting fiber-lends and receiving fiber-lens.

High quality mirrors and high precision mounts are commonly used to guide laser beams with high accuracy and stability. However, the requirements imposed by recent experimental proposals [1]–[3] which will be performed during space missions have raised the technical requirements of the various well-established techniques to an extreme level. As a consequence, manufactured components have even tighter tolerances in order to abide to these stricter requirements. This leads to higher costs and complexity for the fabrication process of the components.

The goal of the approach described in this project is to relax significantly the tolerances of each component and therefore reduce the complexity and subsequently the costs. Instead of tightening the tolerances in order to achieve a mission's requirements, our approach intends to relax them and compensate for any misalignments through the use of novel corrective optics. The beam steering action is achieved by using a pair of wedged

prisms (Risley prisms) and a simple rectangular plate (Figure 1.2). The prisms will cause refraction of the beam depending on their relative angle while the glass plate will displace the beam to the designated position. By rotating the prisms, thus changing the relative angle, the beam can be refracted to the desired direction.

Figure 1.2 Breadboard with corrective optics. A pair of wedges aligns the beam while the plate displaces it.

The aforementioned corrective optics are less sensitive to misalignments and therefore allow us to greatly relax the tolerances of the subcomponents used, especially those of the optical fiber coupler. Using this approach, a complex, multi-component fiber coupler is reduced to a robust monolithic element.

All manufactured components are produced from Zerodur®, a glass ceramic material from Schott that exhibits ultra-low coefficient of thermal expansion (CET) and excellent mechanical and chemical stability. All optical elements will be attached to Zerodur components and the assembled parts will be placed on a Zerodur optical breadboard.

2. Motivation

The accuracy, precision and stability requirements of space mission optical components and systems are always stricter to ensure that maximum optical power transmission is maintained throughout the duration of the space mission. Every component of the system should be able to withstand vast temperature changes, significant doses of radiation, mechanical vibrations and shocks and must exhibit low outgassing in vacuum conditions that are encountered during the launch and the flight of a space mission.

Many space missions include optical systems with fiber - free space - fiber coupling and one of the most crucial and challenging steps is to produce a well collimated and aligned beam at the exit of an optical fiber. Fiber couplers are constructions which serve this purpose. In order to meet the strict restrictions, space qualified fiber couplers are increasingly complex assemblies with even more complex integration processes. Some common requirements are presented in Table 2.1.

Requirement description	**Unit**	**Value**
Surface polish accuracies of components	m	$\lambda/10$
Angular tolerances of components	Arc seconds	2
Angular tolerances of baseplate	Arc seconds	10
Temperature Stability	$K/\sqrt{Hz}$	$1x10^{-4}$
Operating Temperature Range	^{o}C	10-40
Positional alignment	μm	<±100
Beam alignment	μrad μm	<100 <100
Coupling Efficiency	%	>85
Long and short term fluctuations of coupling	%	<5

Table 2.1 Typical requirements for optical breadboards designed for space missions.

Two recent examples of fiber couplers that were developed for specific missions will now be described briefly. For the MAIUS space mission, the proposed fiber coupler is presented in [1]. Most of the parts for this coupler are manufactured from Zerodur, a glass-

ceramic material with low CE which is described in detail in paragraph 4.2. The coupler is composed of three major Zerodur components, the housing, the base and the back plate. Three smaller Zerodur pieces, the brackets, are used to hold the ferrule in place. Lastly, two invar screws are used to push each bracket with um accuracy to position the fiber.

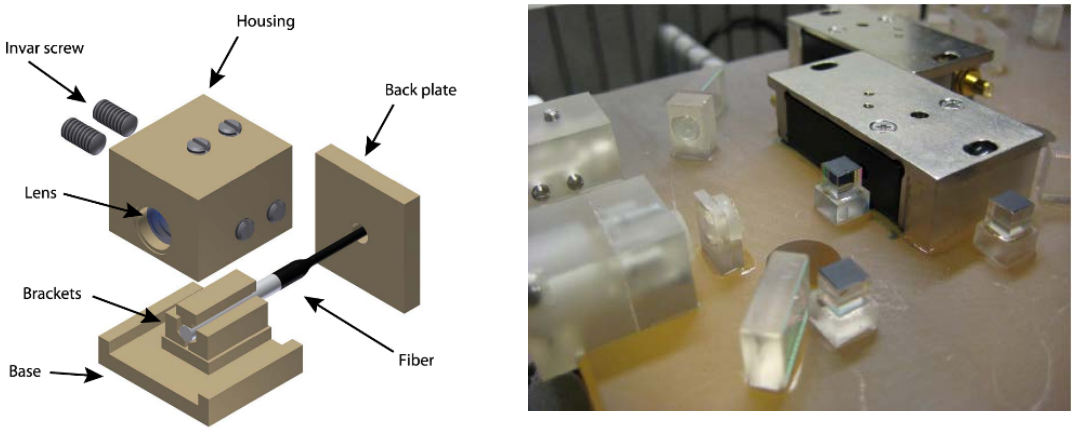

Figure 2.1 Fiber coupler assembly. Left: 3D CAD drawing. Right: Assembled zerodur couplers which are placed on an optical breadboard. Pictures from [1].

In order to assemble the coupler, the ferrule is mounted on three-axis translation stage for accurate positioning. First, the housing and the base are glued to the baseplate using an UV curing adhesive. Then, using the invar screws and the translation stage, the optimum position is found where the ferrule is held firmly. Adhesive is also applied to the brackets and is cured at this point. Finally, the translation stage is removed and the back plate is glued to the rest of the assembly.

For the LISA Pathfinder space mission, a new design of fiber couplers was developed, shown in Figure 2.2 [2]. Bonding between many of the sub-components was performed by hydroxide catalysis and therefore fused silica was the material of choice. Fused silica exhibits low CE and it is ideal for hydroxide catalysis.

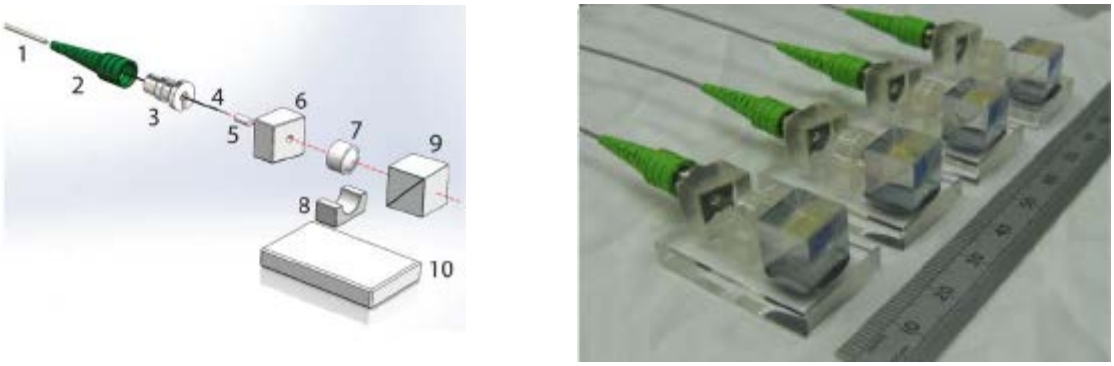

Figure 2.2 Left: Parts of LISA Pathfinder coupler. Right: Assembled fiber couplers. Pictures from [2].

The assembly process begins with stripping the fiber (item 4 in Figure 2.2) and gluing the bare fiber to a quartz ferrule (item 5). The fiber is mechanically supported by a protective PEEK sheath (item 1), a hytrel boot (item 2) to limit bend radius and a titanium stress relief part (item 3). The quartz ferrule is then glued to a mounting block (item 6) using an epoxy adhesive while for assembling items 1, 2 and 3 a different epoxy was used. The mounting block is then joined with the baseplate (item 10) using hydroxide catalysis. An aspheric lens (item 7) is glued on a mounting piece (item 8) which is in turn glued to the baseplate with hydroxide catalysis. Lastly, a polarizing beam splitter (PBS) (item 9) is positioned to clean up the polarization of the beam.

These parts need to be positioned with extreme precision. The alignment requirements are of the order of a few micrometers and in order to achieve such accuracy, actuated positioners are used [4]. Furthermore, the final alignment must be completed within two minutes since that is the required time for the bond to start to form. All parts that are joined with hydroxide catalysis must have surface flatness of ~60nm and 2 arc seconds angular tolerance [5]. One more critical factor of this technique is the requirement of a cleanroom environment for hydroxide catalysis during integration.

In view of the previous techniques, our approach has a dual purpose. Firstly, we seek to reduce the requirements of the manufactured components which are tight with respect to the desired outcome. In order to achieve the desired goals, components must be manufactured with extreme precision which will enable accurate aligning with the methods used so far. Secondly, the complexity of the components must also be reduced to facilitate production. Our approach not only changes the design of the coupler, but also incorporates an innovative idea for aligning the laser beam.

3. Optical breadboard parts

A typical optical breadboard consists of a light source, a number of beam steering optics and devices, maybe some manipulation and modulation of the beam and the detection device for the measurement.

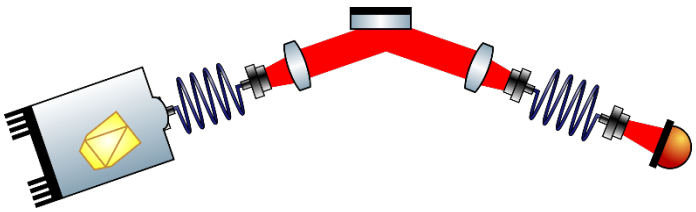

Figure 3.1 Schematic of typical breadboard consisting of a laser source, some optics and at the end a detector.

One of the most common light sources is diode lasers which have many advantages over other types of lasers. They are robust and can operate over a wide range of temperatures and pressures. Also, laser diodes can be purchased at the desired wavelength and power, tailored to the needs of each experiment. But most importantly, the costs of purchase and maintenance are very low.

For guiding the beam, the most efficient steering method is the optical fiber which has dominated the communication and information transmitting networks. Optical fibers are able to guide beams for kilometers with minimum losses. The technology of optical fibers has evolved and produced numerous variations to suit different needs and challenges. Single mode, multimode and polarization maintaining fibers are widely used in many different environments, from research labs to space stations.

Coupling a propagating beam from a laser source into a fiber or from a fiber to another fiber, are common routines, nevertheless non trivial. Maximizing the coupling efficiency (CE), i.e. the percentage of the incident power that is guided through a fiber, requires understanding the physical phenomena involved and delicate handling. Aberrations, fiber misalignments and fiber mode[1] mismatch must all be minimized.

[1] Modes are called the different configurations of electromagnetic waves that can propagate through a waveguide. They arise from solving the Maxwell equation with boundary conditions a cylindrical homogenous dielectric waveguide [39].

Since many applications require, at least partly, free space transmission, alternative methods should be used for beam steering. For free space transmission, efficient beam steering has always been a challenge, where optics on kinematic (ball bearing) and gimbal mounts have been used for decades with a continuous effort to improve their performance. The complexity of these mounts is increasing to satisfy stricter requirements on stability and precision. Substituting a typical mount with a pair of wedges and a glass plate simplifies vastly the system while offering precise and accurate beam steering.

For maximizing the CE, precise alignment is not the only concern. One of the most important technologies used in every optical breadboard is the anti-reflection (AR) coatings which minimize the losses due to reflections from the optical surfaces. They are applied almost on every single optical element to improve performance.

3.1. Light sources: diode lasers

Lasers distinct themselves from other light sources, because they radiate highly directional and coherent light. Lasers exhibit spatial and temporal coherence which allow many applications to be realized that were impossible in the past[6]–[8]. In general, they are divided into solid state lasers, gas lasers, liquid lasers, and plasma lasers, depending on the state of the gain medium[2].

Semiconductor or diode lasers are a special case of solid state lasers. They use different mechanism from the other solid state lasers to achieve the population inversion which is necessary for lasing. In diode lasers, light is emitted due to recombination of electrons and holes in a p-n junction. In a forward biased junction holes and electrons are diffused from the outer layers towards the active region. This diffusion creates the mandatory population inversion for the diode laser.

Obviously, the wavelength of the radiated light depends upon the energy bandgap of the lasing material. The material should be a direct bandgap[3] semiconductor in order to

[2] Gain medium is the section of the laser where light amplification occurs.

[3]Direct bandgap semiconductors have the minimum of the conduction band and the maximum of the valence band at the same value of crystal momentum. Inversely, indirect bandgap materials have their respective minimum and maximum at different values of crystal momentum.

obtain sufficient efficiency. Furthermore, the area that emits light, the active region, should be rather thin to further increase the efficiency. Typical values of the thickness are in the order of 0,1μm.

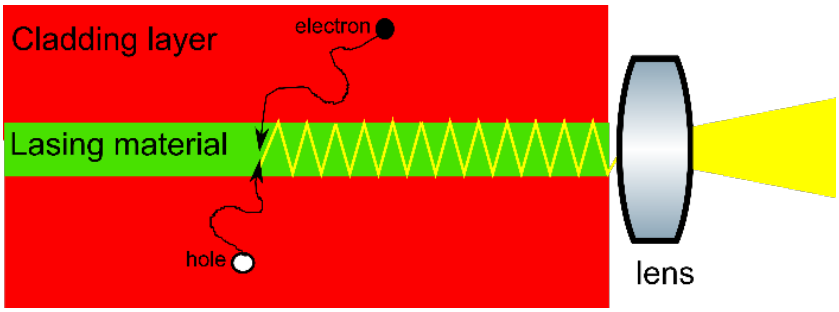

Figure 3.2 Structure of diode laser.

Usually, the lasing material is surrounded by layers with wider bandgap and lower index of refraction, the cladding layers (Figure 3.2). They are usually grown epitaxially on a substrate with thickness about 1μm to ensure that light is adequately confined. Also, the cladding layers provide the carriers, electrons and holes, for the recombination. This form of sandwich serves dual purpose. Firstly, due to the difference in the bandgap a trap is created for the carriers, which makes recombination highly localized and thus efficient. Secondly, because the cladding layers have lower refractive index, a form of waveguide is created which confines light. Additionally, by carefully selecting the dimensions of the layers and therefore those of the waveguide, mode selection is achieved. This kind of structure is called double heterostructure and is the most common for diode laser fabrication.

However, for high efficiency the lattice constants between the active material and the cladding layers must match. Otherwise, non-radiative recombination is increasingly possible. To tackle this problem one common solution is decreasing the dimensions. If the active area has small enough dimensions, approximately 100nm, then quantum effects become important and a quantum well (QW) is created. Here, recombination is possible only through the quantum well and non-radiative recombination is deterred. One QW or multiple quantum wells (MQW) can be employed in a diode laser to acquire the desired features. Even further, quantum dots are used as active areas to increase quantum efficiency.

To complete the main structure, it is essential, as in any laser, to form a resonant cavity. The orientation of the resonant cavity categorizes semiconductor lasers into two big families. If it is parallel to the axis of the layers, it is an edge emitting laser and the most popular variations are Fabry-Perot (FP) and Distributed Feedback (DFB) diodes (Figure 3.3). FP lasers simply have the end faces cleaved to create a cavity. Slicing the layers of the diode perpendicularly to a natural crystal plane creates reflecting end faces, with reflectivity in the order of 0,3 [6]. Since reflectivity of about 0,9 is commonly needed for lasers, applying dielectric coatings to the end faces can modify the reflectivity to the desired levels. For the DFB lasers, a grating of refractive index is constructed parallel to the axis of a cladding layer. This grating must have specific and discrete periodic values to force reflections throughout the optical cavity. Due to Bragg scattering, light only propagates parallel to the axis of the grating.

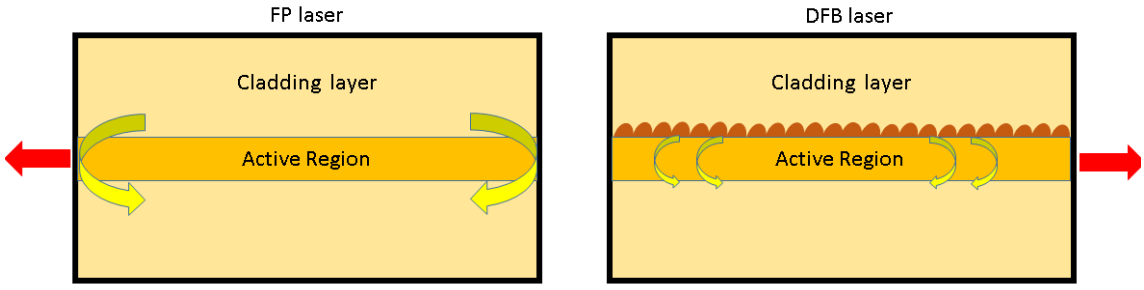

Figure 3.3 Schematic of FP and DFB lasers.

If light is guided perpendicularly to the axis of the layers, a Vertical Cavity Surface-emitting Laser (VCSEL) is formed (Figure 3.4). The cladding layers have large differences in refractive index forming Distributed Bragg Reflectors (DBR). Usually the thickness of each layer is chosen to be a quarter of the targeted wavelength. Hence, two adjacent layers are half the wavelength and light is enhanced. In this case, an FP-like structure is formed on the vertical direction.

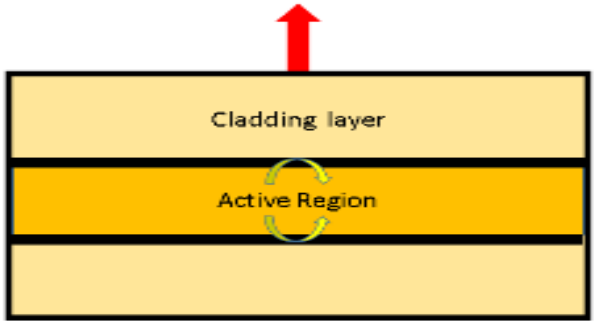

Figure 3.4 Schematic of VCSEL function.

For optical fiber communication light should be emitted almost exclusively in a single transverse and longitudinal mode. To achieve single transverse mode, the thickness of each layer must be carefully selected as well as the index of refraction. Great precision is needed when constructed each layer to comply with the tight tolerances. The dimensions of the active area greatly affect longitudinal single mode transmission and especially the length of the resonant cavity. For single lateral mode short diodes are required which are difficult to fabricate. Using VCSEL or Bragg gratings bypasses this problem and achieves single lateral mode.

The intended output beam of many lasers is a Gaussian beam. The amplitude and intensity distributions of such beams are described by the Gaussian function. These beams match the profiles of optical fiber that are commonly used in many applications and therefore light can be easily coupled into the fibers.

3.2. Optical Fibers

Fibers are dielectric waveguides of light that are capable of transmitting light with very low losses, high bandwidths and are practically immune to electromagnetic interference [9]. Additionally, fibers provide electrical isolation and increased signal security [10]. Those qualities along with their minimal size and weight, as well as the abundance of the raw material, silicon, led to the substitution of the copper wire with optical fibers for the needs of communication.

Fibers consist typically of three parts, the core, the cladding and the jacket or buffer (Figure 3.5). Light propagates inside the inner part, the core, and cannot escape from there.

Due to the incident angle and the difference of the refractive index between the core and the surrounding material, which is called cladding, light undergoes total internal reflection which forces propagation only in the core. Furthermore, the cladding minimizes the distortion of the beam during the propagation. External stress could affect the core and cause distortions in the absence of cladding. Therefore, cladding is generally considered a necessity.

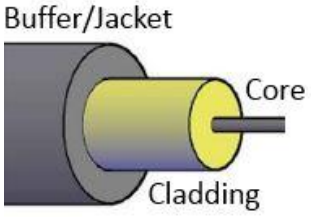

Figure 3.5 Parts of an optical fiber.

The core usually consists of pure silica but depending the desired type of fiber some dopants might be added. Commonly germanium or even rare-earth metals are added and by altering the dopant's quantity, the refractive index and other properties of the fiber can be carefully controlled. It is crucial for the wave guiding ability of the fiber to precisely and accurately determine the refractive index of the core. Hence, the manufacturing method of the core is of paramount importance to ensure the production of the selected refractive index.

The manufacturing commences with the production of a solid glass rod which is called preform. Preform is fabricated from highly pure silicon tetrachloride ($SiCl_4$) plus any desired dopant. One common process employed for the fabrication is the Modified Chemical Vapor Deposition (MCVD). In this process, the chemical reagents are heated by an external heat source inside a rotating tube. The reagents are transported to the heat chamber using a carrier gas stream usually of Ar or Ne. This step exploits the fact that halides like $SiCl_4$ have greater vapor pressure than most contaminants and thus increase the purity of the reagents [11]. Inside the tube, a moving torch fuses the reagents to form a thin glassy layer. The MCVD continues until the desired amount of layers has been deposited and the rod is almost complete, usually between 30-100 layers. The composition and properties of each layer can be controlled in real time, allowing the production of step index or graded index fibers.

In step index fibers (SI), the refractive index of the core is constant and changes abruptly to that of the cladding at the boundary surface. While in the graded index fibers (GI) the core refractive index changes smoothly in a radial fashion. It starts from a high value at the center of the core and reduces gradually to that of the cladding. When the change of the refractive index is approximately parabolic, the conditions are the fittest for propagation of multiple modes. The SI fibers have greater intermodal dispersion than GI fibers but they also exhibit higher coupling.

To finish the production of the preform the tube with deposited material must be then collapsed into a solid rod. The heat is therefore further increased and the reagent supply is haltered. The preform is then tested to compare its properties with the specifications. Finally, another tube is collapsed to the outside of the preform, forming the cladding together with the original tube. The process of MCVD has the advantage of an insulated apparatus which minimizes the concentration of [OH^-] ions which are the main culprits responsible for losses [10].

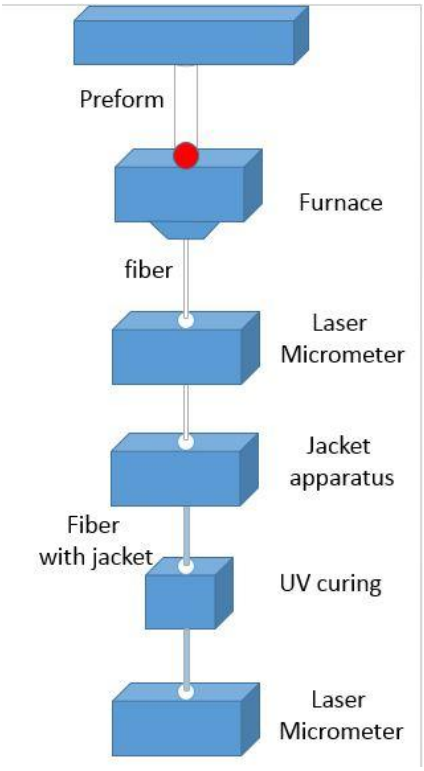

Figure 3.6 Scheme of the fiber draw technique.

When the preform is ready, it must be stretched until the thickness reduces approximately to that of a human hair. This technique is called fiber draw (Figure 3.6). The tip of the preform is vertically inserted into a highly pure granite furnace and is again heated until softening. Then due to gravity a molten drop forms at the tip and stretches until it forms a thin string which is allowed to fall into a laser micrometer. The diameter is measured and checked in relation with specifications. The fiber is then pulled towards the bottom and through an apparatus that is capable of applying various and multiple layers of materials which eventually form the jacket providing mechanical protection to the fiber. The jacket is then cured with UV light and after thorough inspection and testing the fiber is considered complete.

The core diameter can vary significantly from as low as 2μm up to 400μm. Depending on the wavelength intended to be transmitted and the number of modes that will propagate inside the fiber, the core diameter is chosen appropriately. If multiple numbers of modes are allowed to propagate by using larger cores, the waveguide is called multimode fiber (MM). If only one mode may propagate by employing cores between 2-10μm, the waveguide is a single mode fiber (SM). By definition the single mode fibers do not suffer significantly from intermodal dispersion as only one mode can propagate. On the contrary, in multimode fibers, because of the multiple modes that do propagate, intermodal dispersion is present and thus attenuation is increased. On the other side, the increased diameter of the MM fiber core facilitates the coupling of light and especially the coupling of spatially incoherent light. Additionally, the MM fiber connectors are easier to manufacture.

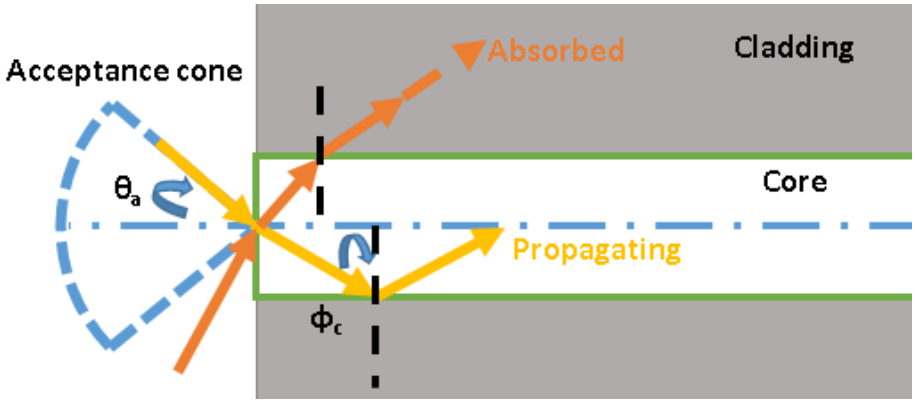

Figure 3.7 Acceptance cone of an optical fiber.

A crucial parameter of a fiber is the Numerical Aperture (NA). Due to the geometry of the fiber, not all incoming rays of light can propagate through the core. Incident rays with an angle higher than a critical value, φ_c, cannot propagate. They are refracted into the cladding and eventually absorbed. On the contrary, incident rays that do propagate, form a cone with a maximum acceptance angle θ_a (Figure 3.7).

Through Snell's law and some geometry, we can derive and define the NA with equation 3.1 [10]:

$$NA = n_0 \, sin\theta_a = \sqrt{n_1^2 - n_2^2} \qquad (3.1)$$

where n_0 is refractive index of the medium before the fiber, n_1 and n_2 are the refractive index of the core and the cladding respectively. With this equation the NA is correlated with the refractive indexes of the core and the cladding. It is worth noting that the difference between the refractive indexes is in the order of 1%. This poses a real challenge for the manufacturing process.

We can estimate the number of modes N that will propagate through a step index fiber with radius of the core r, and wavelength of the travelling light λ, from equation 3.2 [12]:

$$N = 2 \left(\frac{\pi \, r \, NA}{\lambda}\right)^2 \qquad (3.2)$$

For a graded index fiber with parabolic profile we find equation 3.3:

$$N = \left(\frac{\pi \, r \, NA}{\lambda}\right)^2 \qquad (3.3)$$

which is half the modes of the step index. From these equations it is evident that for SM fibers we cannot have both large NA and big core diameters. When increasing the core diameter to facilitate production, the NA must reduce which means smaller difference in the refractive indexes which is harder to achieve. One way around this impasse, is the employment of different index profiles such as triangular or W profiles.

Many applications require the polarization to be constant over large lengths. However, SM fiber due to some minute differences in the core geometry or internal and external stresses exhibit birefringence and alter the polarization. The high rotational

symmetry of the fiber enables the polarization to shift. By breaking the symmetry, fibers are capable of maintaining the same polarization over considerable distances and are called Polarization Maintaining (PM) fibers. In order to achieve that, the main solutions are to exploit the extremes. By minimizing birefringence, the interactions between axes is minimized and therefore the state of polarization is preserved. On the other hand, by maximizing birefringence, the state of polarization cannot change due to the vast difference of propagating velocity between the two axes. Maximizing birefringence is mostly used for practical purposes and it can be accomplished through geometrical shapes or stress effects. The most common structures are referred by bow tie and panda (Figure 3.8). Both use stress rods to maximize birefringence but of different shape.

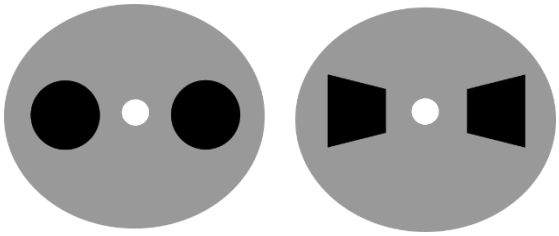

Figure 3.8 Panda (left) and Bow tie fibers (right). The black shapes are the stress rods while white is the core of the fiber.

3.3. Beam Coupling

Coupling efficiency (CE) in an optical system could be defined as the fraction of the input optical power that is transmitted through the system. For the case of a Gaussian beam incident on a fiber, the CE is the overlap of the incident distribution with the Eigenmodes of the fiber. The distribution of the amplitude of the electrical field of a perfect Gaussian beam is given by:

$$\psi = \psi_0 \, exp(-\frac{x^2+y^2}{w^2}) \qquad (3.4)$$

where w is the spot size of the beam and the minimum spot size is the waist of the beam. From the equation, it is evident that fiber misalignments, fiber mode mismatch, and aberrations can affect the CE [13].

Mode mismatch is largely due to significant waist differences which are determined from the active area of lasers and core diameters of fibers. Therefore, laser to fiber coupling is inherently different from fiber to fiber coupling due to large differences in active areas. In the first case, in order to achieve significant CE, the light emitting area should be equal to or smaller than the fiber core (p.17.13 [14]). Depending therefore on the laser source this constraint frequently cannot be met and CE never exceeds certain values. In fiber to fiber coupling the above mentioned constraint is easier met. The differences in core diameters are negligible between SM fibers and high CE can be routinely achieved with accurate alignment.

Apart from the core diameters, the alignment affects vastly CE. For a simple fiber-fiber connection, extreme accuracy is needed when positioning each fiber, since a few micrometers of lateral displacement, of the order of 5~10um, can result in total power loss (p48 [15]). CE is not as sensitive to longitudinal displacement, where several hundred micrometers are required for total power loss. Furthermore, the angular positioning of the fiber is also crucial since tilting a fiber as little as 50mrad imposes significant losses to the system [15].

To increase the accuracy of alignment, fiber couplers are commonly used. Fiber couplers (Figure 3.9) are commercially available components that usually have well defined lateral position of the fiber and minimize the angular misalignment. They include a collimating lens and, in some cases, the longitudinal displacement of the fiber is also fixed, while in others it can be tuned. Therefore, collimation of the beam can be either predetermined or optimized.

Figure 3.9 Typical fiber coupler

When the system is not a simple fiber-fiber connection, but involves free space propagation and several optical elements, alignment becomes harder and more complicated. Each element must be positioned and aligned with micrometer accuracy, in most cases.

3.4. Optical elements

The optical elements used in the system that will be build are a pair of wedged prisms and a glass plate. Wedged prisms, or Risley prisms have been used by ophthalmologists to measure binocular accommodation. That is the ability of the optical axes for the two eyes to converge for nearby objects and therefore were typically manufactured with small angles. However, recent developments have increased the angle range and achromatized prims, permitting thus their use in many steering applications.

A wedged prism causes a refraction of the beam depending on the angle of the prism. If two identical wedges are positioned parallel to each other, the total refraction is twice the angle of each one, acting as a single prism with twice the angle. By rotating the prisms together, the beam is rotated on a circle (ω angle in Figure 3.10). If the prisms are rotated relative to the other, the beam can point anywhere inside the circle until the wedges are positioned in a such a way that the total beam deviation is zero, acting like a parallel plate.

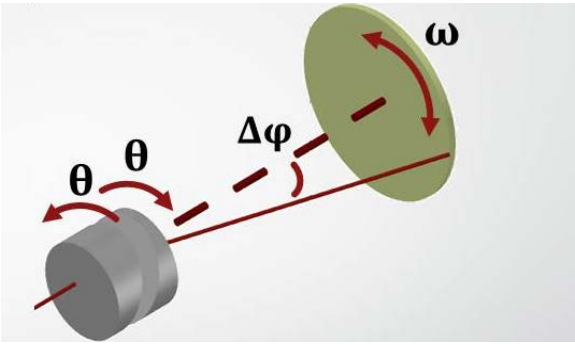

Figure 3.10 Beam deviation due to a pair of wedged prisms.

When propagating in air, the beam is refracted by the pair of prisms following equation 3.5:

$$\Delta\varphi = \frac{4}{\pi}\,(n-1)\,\alpha\,\theta \qquad (3.5)$$

where θ is the angle that each of the wedge is rolled but in opposite directions, a is the angle of the wedge, and n is the refractive index of the wedge. Because of the way wedges operate, they are relative insensitive to vibrations which is important for space missions.

A glass plate only causes a displacement of the beam depending on the relative angle between the plate and the incident beam. The adjustment of the angle displaces the beam by an amount Δh which for small angles can be calculated by equation 3.6:

$$\Delta h = \theta\, d\, \frac{n-1}{n} \qquad (3.6)$$

where θ is the angle that the angle plate is tilted, d is the thickness of the glass plate and n is the refractive index of the glass plate.

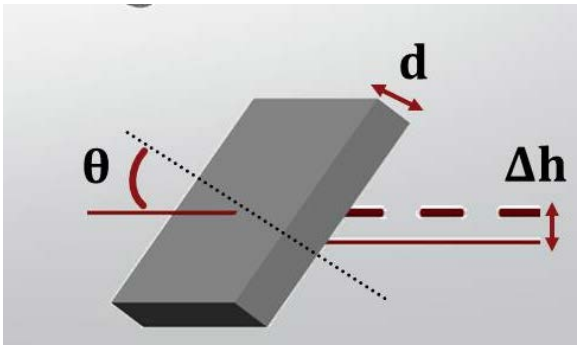

Figure 3.11 Beam displacement due to a glass plate.

3.5. Anti-reflection coatings

In general, optical coatings are applied to modify the optical properties of a surface. Anti-reflection (AR) coatings are used to reduce the Fresnel reflection and in some case to increase transmittance. They may consist of one or a few transparent nano-layers of dielectric materials with different refractive indices. In the case of single layer, a common design is to produce a layer thickness of λ/4n, where λ is the targeted wavelength and n the is the refractive index of the layer. The refractive index, n, is chosen such that it corresponds to the value given by equation 3.7[16]:

$$n = \sqrt{n_1 n_2} \qquad (3.7)$$

where n_1 is the refractive index of the medium before the coating while n_2 is the refractive index of the material after. In the case of multiple layers, successive predefined layers form a structure which through many interferences produce low reflection losses.

AR coatings are conveniently separated into two categories; those with high index substrate which apply mainly for infrared (IR) radiation and those with low index substrate which are for the visible spectrum. Since the region of our principal interest lies in visible spectrum we shall focus on the low index substrate.

Popular materials for substrates, like silicon (n=3,5) and germanium (n=4) have high refractive indices. When designing AR coatings for the visible spectrum finding a suitable substrate could be a problem. The lowest practical index is found in magnesium fluoride (n=1,38 for λ=500nm) but in most cases crown glass is used (n=1,52) [17]. The layers that are deposited on top of the substrate are usually zinc sulfide, cryolyte and even silver in some cases.

Depending on the production method coatings are also classified as soft or hard coatings. When producing soft coatings, the layers are laminated together in a vertical stack while for hard coatings, plasma deposition is used for creating the layers. Plasma deposition is performed more accurately as the growth rate of layers is controlled up to single atoms. Therefore, hard coatings exhibit homogeneity which leads to decreased transmitted wave front error and increased temperature and humidity stability. Furthermore, the optical performance is enhanced since optical scattering is reduced and transmission is increased [18].

Furthermore, when designing an AR coating the angle of incident light is a concern. In some applications only normal rays are important while in others random orientation is also taken into account. Coatings can then be designed to reduce reflectance at some angles other than normal incidence [19].

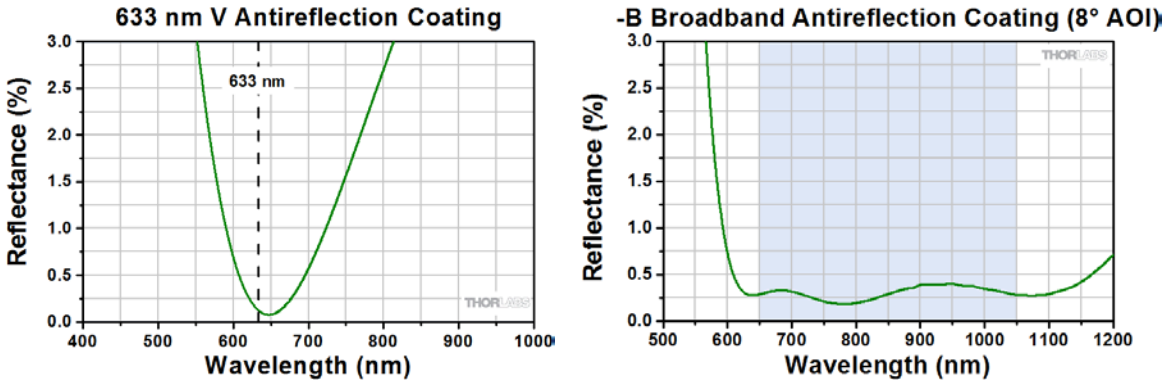

Figure 3.11 Performance of V and B coating respectively from Thorlabs.com.

The AR coating could be designed to suppress reflections over a narrow bandwidth of the spectrum. These are called V-coatings from the shape of the curve of the spectral reflectance which has only one sharp minimum approaching 0% reflectance at the design wavelength. On the other hand, if wider bandwidth is needed, the curve exhibits two minimums over a wider area and they are named as B-coatings. If we compare the absolute minimum reflectance between them, then the one of the V coating is lower than that of the B-coating.

4. Adhesives and materials

4.1. Adhesives

A number of different adhesives based on various technologies were explored. Since adhesives would be the only technique used to connect each and every piece of the breadboard, it is highly important to investigate the maximum amount of options.

Adhesive bonding is a well-established technique for jointing optic elements [20], [21]. Adhesives with high viscosity are usually preferred since they are more easily applied. UV curing adhesives provide the advantage of increased aligning time. When using epoxy or HC bonding, there is a limited amount of time before curing begins. However, for UV curing adhesives, the process only begins when light shines on the adhesive. Furthermore, adhesive bonding has been compared to HC bonding for thermal and mechanical stability (Figure 4.1). The performances of both were comparable and thus adhesive bonding can be used in experiments for space missions [22].

Figure 4.1 Zerodur plate that was used to compare HC to adhesive bonding. Picture from [22]*. Top left and bottom right Zerodur pieces were attached to the plate using adhesive bonding while the rest were attached using HC. The whole plate was subjected to thermal and mechanical tests.*

Thermoplastic adhesives are an interesting option. The bond that is created can be softened by heating the adhesive and thus permitting easy removal or adjusting of a component.

4.1.1. UV curing

Adhesives that cure with ultraviolet light have considerable advantages. They are a one-part system that does not require any other action, like mixing or heating, apart from the curing process. Furthermore, the time of the initiation of the cure is selected by the user, supplying practically infinite amount of time for performing alignment of optics or any other operation.

Two families of commercially available adhesives were tested. The first group of adhesives are optical adhesives especially designed for bonding optical elements. The second group of adhesives are designed for dentical use and they provide the advantage of curing in a different wavelength from the optical adhesives.

Norland Optical Adhesives®

Norland Optical Adhesives® (NOA) are widely used in the optics industry. They are usually clear, colorless, liquid and UV curing photopolymers. Curing time depends on the thickness of the applied glue, the power and the spectrum of UV light available. Maximum absorption is achieved within the range of 320-380nm, with peak sensitivity around 365nm depending on the particular adhesive. Three products of Norland were used in the experiments NOA 61, NOA 63 and NOA 88.

NOA 61 is a mercapto-ester which is cross-linked, when polymerized, by a triallyl isocyanurate. Mercapto-esters react vigorously with metals and ions. NOA 61 is manufactured such as to create a strong optical bond between glass surfaces, metals, fiberglass and glass filled plastics. Moreover, it complies with Federal Specification MIL-A-3920 for optical adhesives and can be used in all government contracts requiring such adhesives. It is usually used for bonding various optical elements as well as for terminating and splicing optical fibers.

Furthermore, NOA 61 exhibits high clarity and low shrinkage when cured. These features enable the assembly of high quality optical systems with stable performance over long periods of time. The manufacturer recommends for full cure, a fluence level of 3 Joules/cm^2 for the aforementioned wavelengths. It is also important that cure is not

inhibited by oxygen but the adhesive itself oxidizes with oxygen when the container has been opened. Therefore, after opening a container, the adhesive is no longer effective after a month due to oxidation.

After fully curing NOA 61, it is recommended to age the bond over a time period of about 1 week, during which a chemical bond is formed between the substrate and the adhesive. This process can be accelerated by heating the bond at 50° C for 12 hours.

NOA 63 is another excellent adhesive for use with optics. The characteristics of this adhesive that stand out are high viscosity, low fluorescence and excellent transmission in the near UV range. After complete curing, the adhesive exhibits high transmission in the range from 320 to 3,000 nm. Additionally, NOA 63 bonds firmer glass and metal.

NOA 88 was designed as a low outgassing material, with a low collected volatile condensable mass (CVCM), and low total mass loss (TML) adhesive. This adhesive is recommended for any assembly manufactured for space exploration and in general for sensitive electronics or optical components.

Properties	**NOA 61**	**NOA 63**	**NOA 88**
Viscosity at 25^{o}C (cps)	300	2000	250
Refractive Index of Cured Polymer	1.56	1.56	1.5
Elongation at Failure	38%	6%	41%
Modulus of Elasticity (psi)	150,000	240,000	131,000
Tensile Strength (psi)	3,000	5,000	2,000
Hardness - Shore D	85	90	90
CTE (10^{-6} /^{o}C)	220	220	220
Shelf life	4 months	6 months	4 months

Table 4.1 Comparison of properties for different Norland optical adhesives, from [23].

The CTE of the NOA adhesives that will be used are almost identical and their difference in the region of 0-50^{o}C is negligible (Figure 4.2). The CTE in this region is about 220 x 10^{-6} / ^{o}C and their glass transition temperature (Tg) is 30^{o}C before curing. After curing they can withstand temperatures from -15 up to 60^{o}C. If after curing the bond is left to age for a week when the bond acquires full strength, it can then withstand temperatures from about -150^{o} to 125^{o}C. Their properties change very little above Tg, where they become a little bit softer as expected. These adhesive are made from a urethane related base material and behave different than epoxies and acrylates. They are more flexible and resilient which means that they can handle better the stresses and forces that might be created.

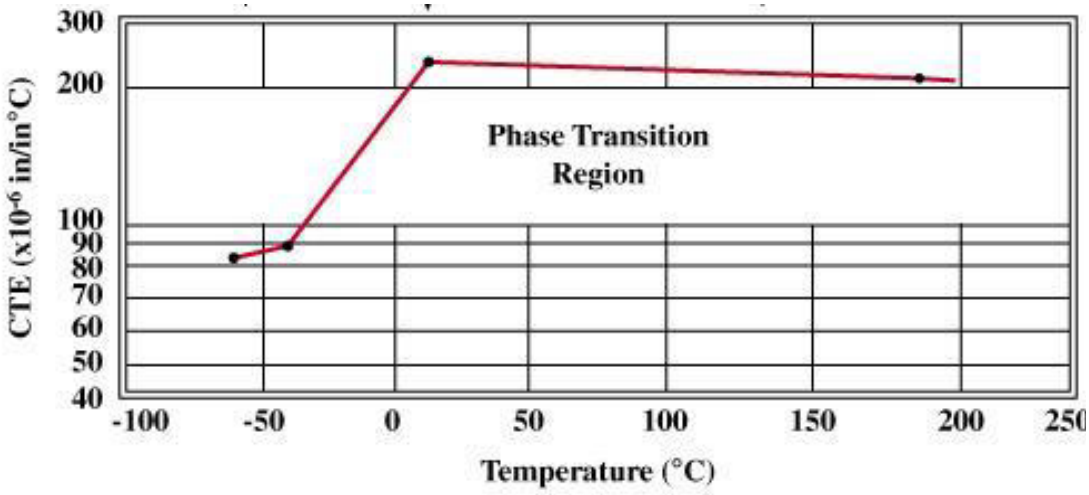

Figure 4.2 CTE of NOA adhesives over a range of temperatures, from [23].

The spectral transmission of adhesives is another important factor. For these NOA adhesives, the transmission is high in the region of interest (around λ=780nm). In Figure 4.3, Figure 4.4, Figure 4.5, the spectral transmission for NOA 61, 63 and 88 respectively are presented.

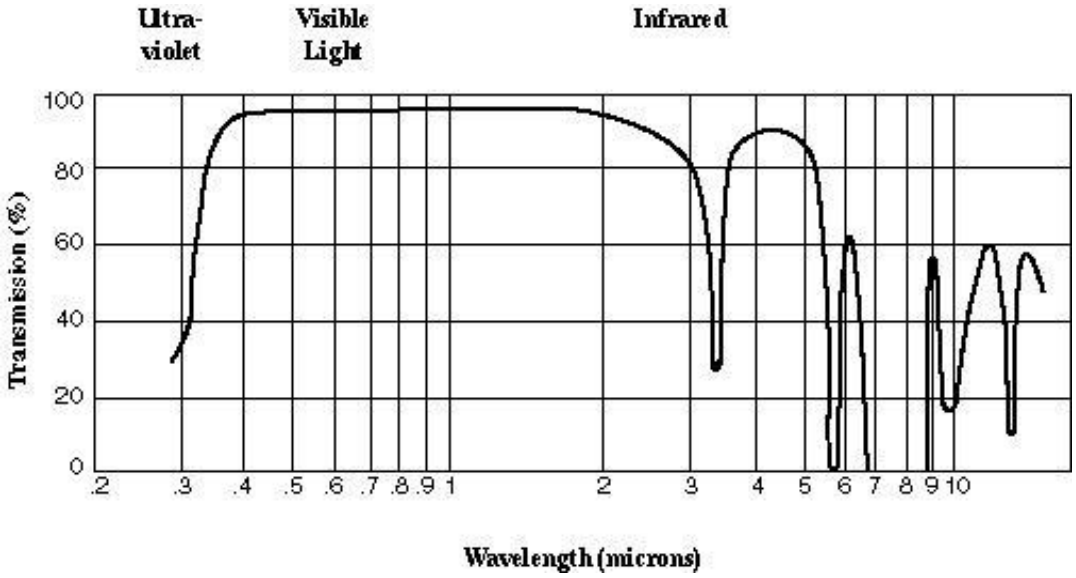

Figure 4.3 Spectral transmission of NOA 61, from [23].

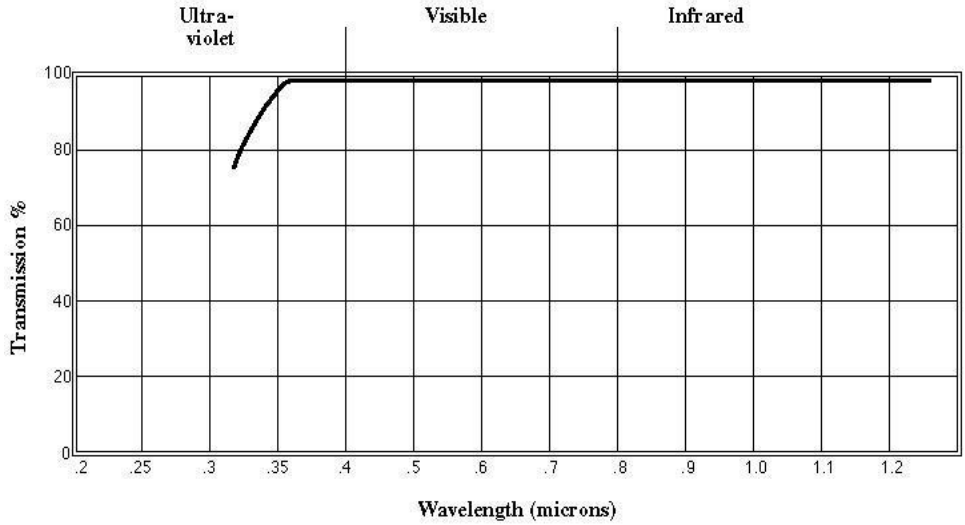

Figure 4.4 Spectral transmission of NOA 63, from [23].

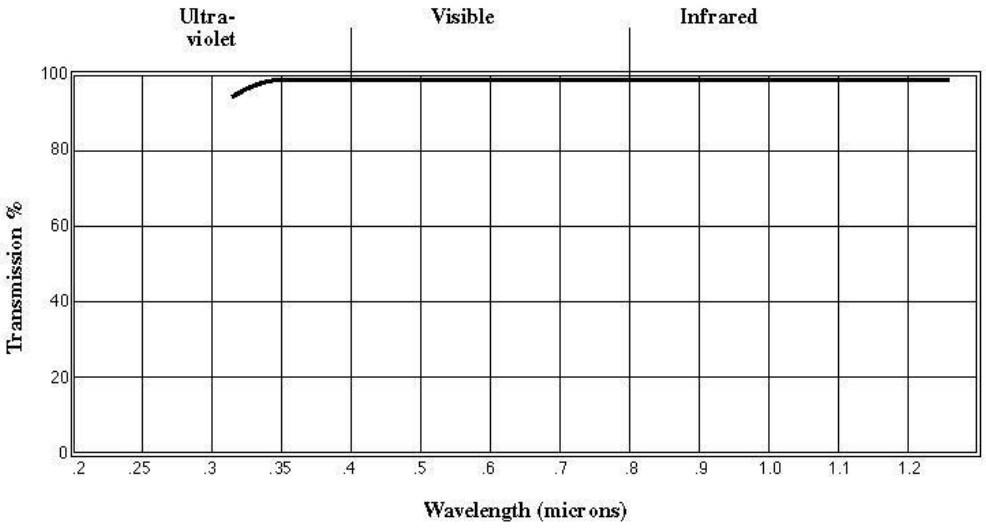

Figure 4.5 Spectral transmission of NOA 88, from [23].

Prevest Denpro®

Prevest Denpro® manufactures dentistry products. The adhesives that are used in dentistry, cure at different wavelengths from the common adhesives used in opto-mechanical or in electronic applications. One option would be Fusion Flo adhesive that has already been used with optics and Zerodur [1]. Fusion Flo has a nano flowable composite which delivers high strength and wear resistance. Furthermore, it is characterized by optimum surface affinity. It has a flexural strength of 135 MPa, Polymerization Shrinkage 3.3 Vo.%, Modular of Elasticity 9490 MPa, Curing Depth 3.5mm, Abrasion 34um[4]. This adhesive cures when illuminated with light at 460nm.

Its composition involves silanated barium glass powder with particle sizes that vary from 20nm to 2um and silica powder with particle sizes from 20nm to 70nm.

3M

An alternative to Fusion Flo that was explored are the products from 3M. Transbond™ Supreme LV (Low Viscosity) Light Cure Adhesive is a flowable orthodontic adhesive. Its composition of nanofillers grants excellent strength, flow and wear properties.

[4] These data were acquired by personal communication with the manufacturer.

The nanofillers are silica and zirconia nanocrystals with average particle size that vary from 5 to 75 nm [24].

It can be used to bond glass with metal or with ceramic materials as well as glass to glass. The adhesive can be cured with light from 450 to 470 nm with peak absorption at 460nm.

4.1.2. Thermoplastic

Crystalbond®

The Crystalbond®, 509 and 590 are thermoplastic adhesives and are ideal materials for mounting objects that require machining processes or constant adjustment. A strong bond is created at room temperature while when heated to the softening point, bond can be relative easily broken. For applying these adhesives, they should be heated to melting point where they flow. Furthermore, these adhesives exhibit high bond strength and adhere readily to metals, glass and ceramics.

Characteristics/Product	**509**	**590**
Solvent	Acetone	Methanol
Color	Amber	Brown
Flow/Melting Point (°C)	121	150
Viscosity at Flow Point (cps)	6000	9000
Softening Point (°C)	71	125
Weight (gr/stick)	90	227

Table 4.2 Properties comparison for CrystalBond 509 and CrystalBond 590, from [25].

4.2. Low CTE Materials- Zerodur

The research for materials with low Coefficient of Thermal Expansion (CTE) boomed when it was noticed that the crystal structure β-eucryptite exhibits negative CTE [26]. This structure can be achieved with the so called LAS system (Lithia-Alumina-Silica), which has been thoroughly studied, for ratios around 1:1:2.

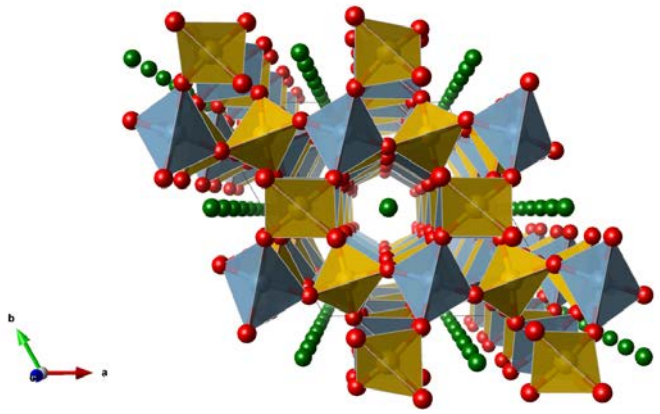

Figure 4.6 β-eucryptite crystal structure with orange being atoms of Al, green Li^+ and red O [21] .

Many different materials have been produced following this formula but for high quality optical application the most successful is Zerodur®. Much of the success is due to its excellent homogeneity of properties [27], high striae quality [28] and low concentration of bubbles and inclusions [29]. These attributes of zerodur reduce the degradation due to radiation which is critical for space missions.

Zerodur is well known for its ultra-low CTE, which results from its unique structure. It is widely used for manufacturing reflectors for telescopes and optical mirrors substrates [30] including the 4m mirror blank for the Calar Alto Observatory in Spain, the 8 m telescopes ESO-VLT the 10 m telescopes KECK I and II, GRANTECAN, and in the x-ray satellite telescopes RO-SAT and CHANDRA [31].

Figure 4.7 Primary mirror in Gaomeigu observatory, Schott.com.

Its composition is glass-ceramic, which means that both amorphous and crystalline phases are present in the material. The crystal phase is formed by crystals, which are about 30-50nm in diameter, and they are suspended in the amorphous material. The amorphous phase has a positive CTE, but the crystalline phase has a negative CTE. By carefully controlling the manufacturing process, the ratio of the two phases is selected to be 70% crystals and 30% amorphous glass. At this ratio the net CTE of the material is essentially zero when a specific chemical composition is applied (Table 4.3).

Chemical element	**wt %**	**mol %**	**CTE change**
SiO_2	55,4	63,9	
Al_2O_3	25,4	17,2	Strongly negative
Li_2O	3,7	8,5	
Na_2O	0,2	0,2	
K_2O	0,6	0,5	
MgO	1	1,7	strongly positive
ZnO	1,6	1,3	slightly negative
P_2O_5	7,2	3,5	No effect
TiO_2	2,3	2	Nucleating agents
ZrO_2	1,8	1	
As_2O_3	0,6	0,2	

Table 4.3 Chemical composition of Zerodur and the effect of each element on the CTE, from [32] , [33].

Zerodur has a low transmittance relative to most glasses [34]. This is also due to the two-phase structure of Zerodur, because light undergoes Rayleigh scattering by the embedded crystals.

Amongst many properties, Zerodur has excellent homogeneity of CTE throughout an entire piece, enabling optomechanical engineering solutions with long-term mechanical and thermal stability. Individual pieces can be manufactured with a mean CTE, α (in the temperature range 0°C to 50°C) in three main expansion classes, as follows in Table 4.4.

	Expansion class 0	Expansion class 1	Expansion class 2
α (10^{-6}/K)	0± 0.02	0± 0.05	0± 0.10

Table 4.4. CTE for different expansion classes, from [29].

The CTE does not change significantly with temperature, especially in the range of 0-100°C. In Figure 4.8 the change of CTE over a wide range of temperatures is shown. However, if Zerodur is heated above 100 °C and the subsequent cooling rate is faster than production rate, then a permanent change can occur on the CTE. For every factor of 10 difference the CTE change can be up to 0.025x10^{-6} /K [35].

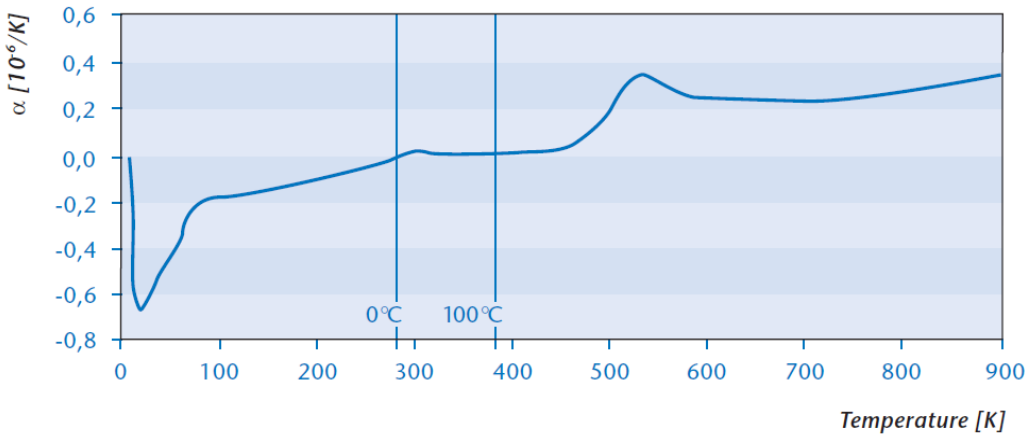

Figure 4.8 Coefficient of linear thermal expansion as a function of temperature, from [29].

4.3. Bonding technique

For creating a bond between surfaces a specific technique was used. Before applying any adhesive, the surface should always be thoroughly cleaned. Typical surface cleaners are methanol, acetone and isopropanol. The aim is to remove all particles and oils or fat that may be present on the surface. If some particle remains after cleaning, it can act as a pressure point for the bond and create cracks [36]. As a result, the bond will be significantly weakened.

For increased bond strength, the amount and the method of applying the adhesive are also important. The thickness of the layer of the adhesive is typically below 20 micrometers. Therefore, depending on the surfaces that will be jointed, the volume should be calculated and applied meticulously. If one of the surfaces can be pressed onto the second, a single drop of the adhesive should be applied to the surface. When the surface is pressed, the adhesive will spread uniformly without air bubbles. If the surface cannot be pressed, then the adhesive must be spread across the surface with a suitable tool.

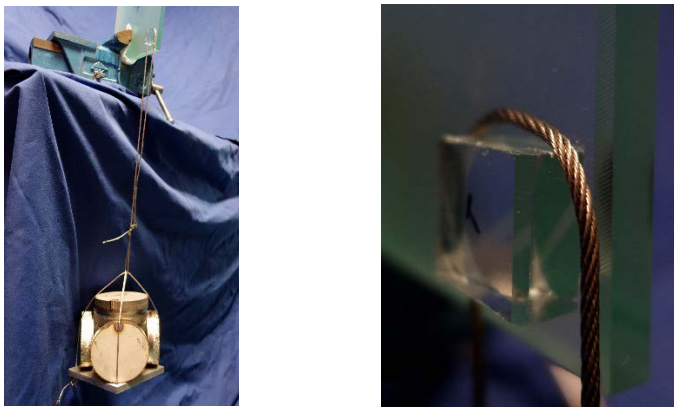

Figure 4.9 Weights hanging from a glass plate using metal wire.

The different types of adhesives that are aforementioned, were tested each one with its own merits. Several glass blocks were joint with a glass breadboard using the afore mentioned UV adhesives. All of them, exhibited strong bonds between glass. They were able of withstanding shear forces of about 100N. For applying these forces, weights were hang from the blocks using metal wire (Figure 4.9). The weights were applied to the blocks for a

short period of time (2-3 minutes) on consecutive days. Specifically, for NOA61 weights have been applied for over 6 months without any sign of the block of breaking, cracking or drifting. However, no significant gain was observed from the use of multiple UV curing adhesive. Therefore, it has been decided to simplify the process by using only one UV curing adhesive. Since, NOA61 has already been tested for military and space applications it will be used for all components.

Furthermore, from the two thermoplastic adhesives, Crystalbond 509 was chosen. Softening and flow temperature are significantly lower than those of Crystalbond 590. Thus, the possibility of affecting another component while heating the thermoplastic adhesive until the softening is reduced.

4.4. Adhesive Removal

Being able to remove cured adhesive is very important. The process of removing cured adhesive was investigated. First, NOA61 was cured on acid treated glass samples. Afterwards, the samples were immersed into a bath of a solvent for two days. Initial tests were performed with common cleaning solvents such as methanol, ethanol, isopropanol and acetone. These solvents did not succeed in removing significant portions of the cured glue in the given time. The next step was to prepare a solution made by methanol, ammonia and methylene chloride (15/2/100 per weight) which is the same solution as a commercially available paint remover. Both of them, homemade solution and commercial paint remover, were applied on individual samples. After 2 days in the solvent bath, both succeeded in removing the cured adhesive. However, paint remover was slightly more efficient and a lot easier to obtain.

Figure 4.10 Zerodur block inside a bath of chromic acid.

Nevertheless, the paint remover nor the homemade solution had the same results on Zerodur. Possibly due to the metal ions present in zerodur, Li^+ mainly, the bond strength is greater and the cured adhesive cannot be removed as easily. The outcome was minimal adhesive removal and zerodur cleaning required more drastic measures. Chromic acid was employed, which is used for cleaning glass flasks and containers in chemistry laboratories (Figure 4.10).

On a zerodur block, NOA61 adhesive was cured. Following that, the zerodur block was immersed into a chromic acid for one day. To verify the removal of the cured adhesive from the zerodur block, the surface quality was checked using a Leica DMRM microscope with a Sony DFW V500 camera. The removal of the adhesive was evident (Figure 4.11) and complete from the entire zerodur block.

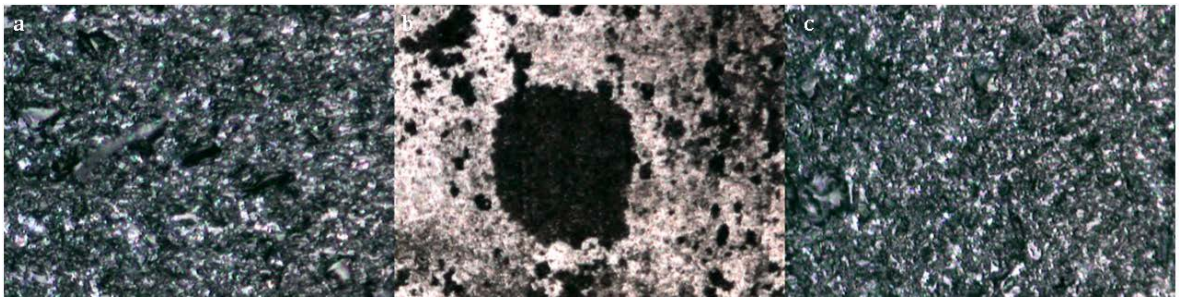

Figure 4.11(a)Zerodur surface before applying any glue. (b) Zerodur surface after application of glue (pink portions of the image) (c) Zerodur surface after bath in chromic acid for 1 day.

The results of our research for removing adhesive from simple glass and Zerodur are summarized in the following table.

Solvent	Glass	Zerodur
methanol, ethanol, isopropanol and acetone	Unsuccessful	Unsuccessful
Solution (NH_3,CH_3OH, CH_2Cl_2)	successful	Unsuccessful
Paint remover	successful	Unsuccessful
Chromic acid	successful	successful

Table 4.5 Summary of solvents tested on glass and Zerodur.

The zerodur block that had been cleaned, could be reused if the surface had not been etched by the acid. To verify that the chromic acid does not etch zerodur, a sample spend 10 days inside a chromic acid bath. The acid did not etch the surface as can been seen in Figure 4.12.

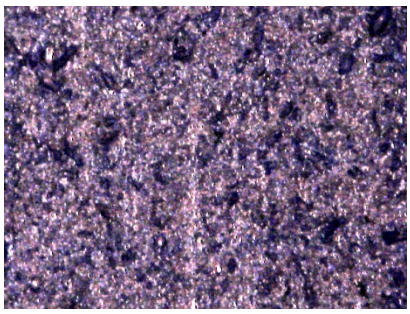

Figure 4.12 Microscope picture of the zerodur sample after spending 10 days inside chromic bath.

5. Optical System Characterization

Before assembling a breadboard, the optical components should be characterized to ensure that the components are within the specifications and can be used in a set up. Moreover, measuring the exact properties of optics, allows to choose which items will be used. Especially for the case of wedges, forming pairs of wedges with practically the same angle is extremely practical, since it is then possible to produce zero displacement of a beam after passing through a pair of wedges.

Since the characterization refers to the confirmation that the tested components are within specifications, it was not necessary to perform absolute measurements of surface roughness and curvature but differential ones by comparing to optical flats. The differential measurement approach outweighs the absolute since it is simple and straightforward without strict technical requirements on optics, beam quality or alignment. A drawback is that a relative value of surface curvature is measured, as compared to the reference optics used. Also, only an upper value of surface roughness can be estimated. On the other hand, such measurements are sufficient to confirm that an optical component is within specs.

The optical metrology apparatus which was used to characterize the optic elements was an interferometer.

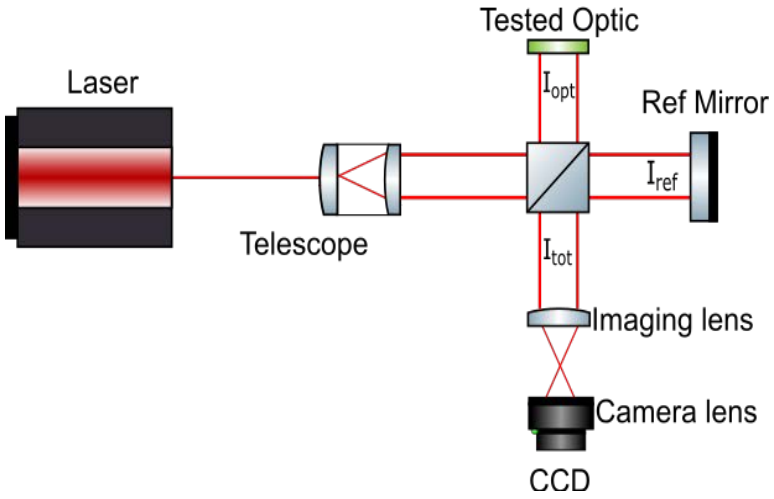

Figure 5.1 Schematic of Twyman Green Interferometer.

The setup is based on a Twyman-Green type interferometer, as shown in Figure 5.1. The set up consisted of a He-Ne source at 633nm, a beam expanding telescope, a 50/50 non polarizing beam splitter, neutral density filters, a reference mirror, an iris, an imaging system consisting of a f=100mm plano-convex lens, a lens system (Pentax C1614-M) and a CCD camera (Imaging Source DMK 21 BU04) (for details see Figure 5.2).

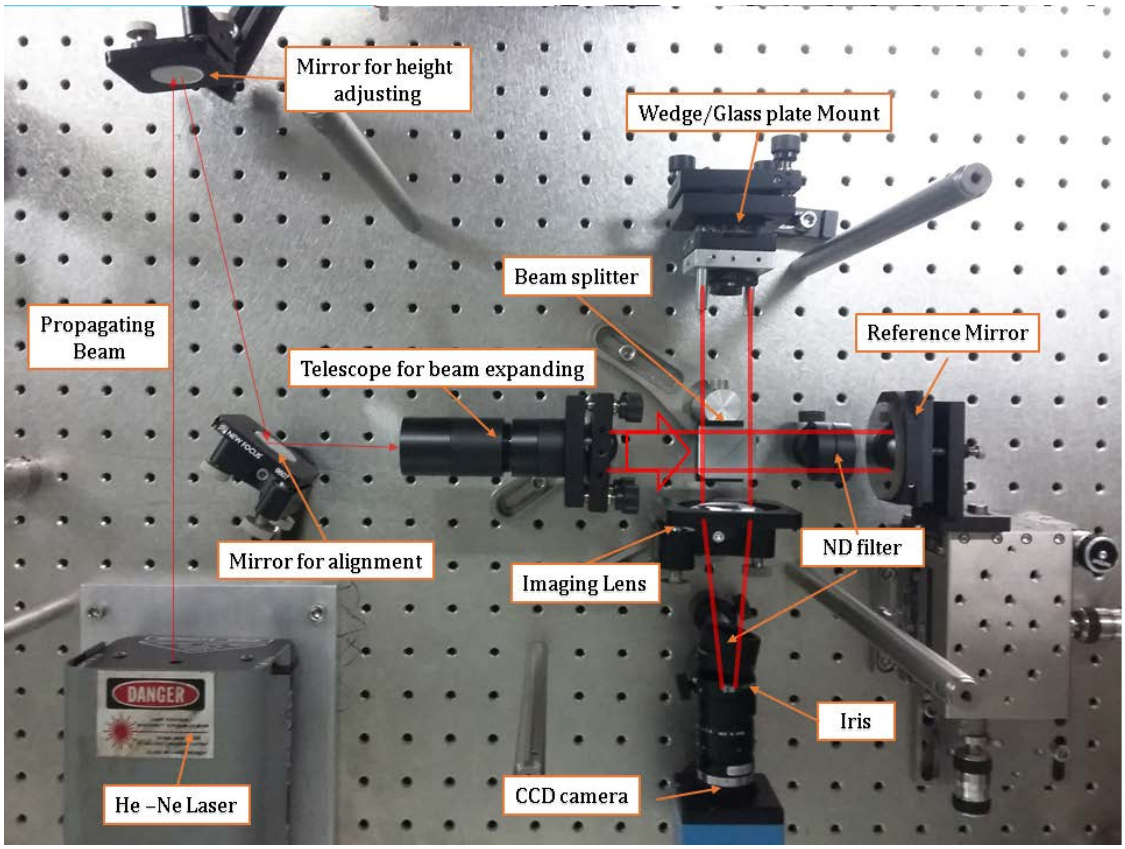

Figure 5.2 Optical metrology experimental apparatus. Guidelines indicating light path along with the various components of the Twyman Green Interferometer are shown.

The differential measurement procedure begins with two flat reference mirrors of equal or better surface quality than the target values (target values: $\lambda/4$, reference mirrors: $\lambda/10$ or better) being placed in the two arms of the interferometer and acquiring an interferogram. This interferogram represents the phase difference of the wavefronts emanating from the two arms of the interferometer. The intensity is maximum (bright fringe) when the two waves are in phase (0 or a multiple of 2π phase difference) while the intensity is minimum when the two waves are out of phase (π or an odd multiple of π phase

difference). By analyzing this interferogram, the distribution of the phase difference of the two reference wavefronts i.e $\Delta\phi_o$ is retrieved. The long spatial range phase variations represent the reference curvature of our mirrors, R_{ref}. By filtering out all long spatial range phase variations, an upper estimate of the surface roughness of our reference mirrors can be retrieved. It should be noted that this measurement is also influenced by the statistical variation of the intensity of the beam, i.e. the beam quality. Although the estimated phase variation leads to an overestimation of the surface roughness it can be used as a reference value.

In the second step, one of the reference mirrors is replaced with one of the optics under measurement and a new interferogram is retrieved. By analyzing this new interferogram, a phase distribution is calculated which represents the phase difference between the reference and sample wave fronts i.e $\Delta\phi$. By subtracting the phase distribution retrieved in the first step of this process $\Delta\phi-\Delta\phi_o$, the clear effect of the sample surface is retrieved, eliminating for example any residual wave front curvature in the original beam. From this differential measurement, the lower value of the radius of curvature of the sample surface and an upper value of the surface roughness are estimated.

On one arm, a reference reflecting mirror is used, while in the other the optics under test are placed. The optical path length between the optical component to be characterized and the imaging lens was d=100mm to match the focal plane of the imaging lens and minimize aberrations.

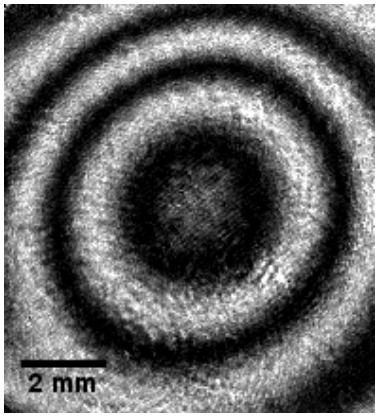

Figure 5.3 Typical interferogram as captured from the CCD.

In more detail, the experimental process begins by measuring the intensity profile incident at the camera sensor. The two waves, one from each arm of the interferometer, are recombined at the beam-splitter and the interference is depicted on the CCD sensor as intensity variations. From this interference pattern, I_{tot} (Figure 5.3), the surface of the optical component under test can be characterized. The measurement procedure continues with blocking the arm of the optical component under test and measuring the reference intensity profile, I_{ref}, which is reflected by the mirror and arriving at the sensor. Then similarly the arm of the mirror is blocked and the intensity of the sample reflection, I_{opt} is measured. In general, the intensity distribution of the interference pattern depends on the intensity distributions of the two wavefronts and their phase difference Δg(r) as described by the following equation 5.1:

$$I_{tot} = I_{ref} + I_{opt} + 2\sqrt{I_{ref} I_{opt}} \cos\left(\Delta g(r)\right) \qquad (5.1)$$

By solving (1) for the phase difference $\Delta g(r)$ we get equation 5.2:

$$\Delta g(r) = arccos\left(\frac{I_{tot} - (I_{ref} + I_{opt})}{2\sqrt{I_{ref} I_{opt}}}\right) \qquad (5.2)$$

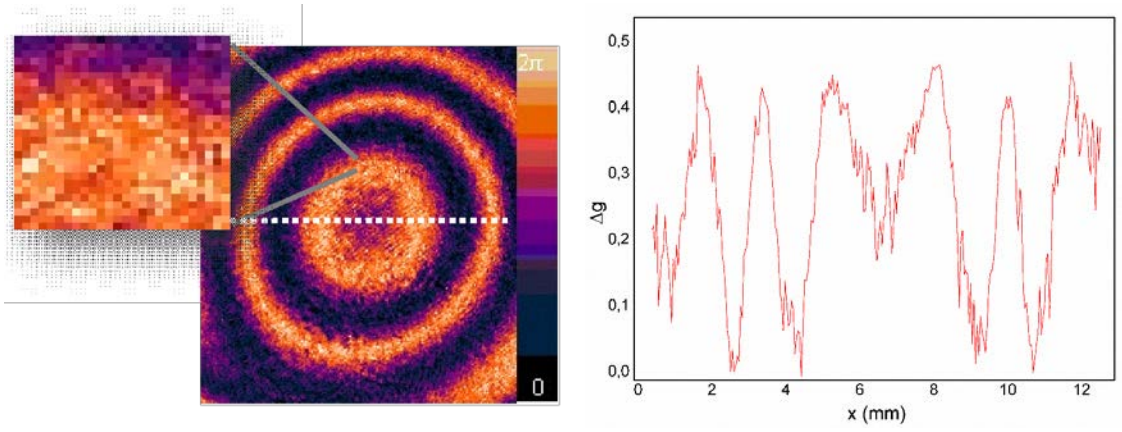

(a) **(b)**

Figure 5.4 (a) Estimated phase distribution in false colors (typical values). Inset: detail of the granular texture of the phase distribution. (b) Phase values along the dotted line in (a)

A typical phase distribution is shown in Figure 5.4. From this distribution we quantitatively extract two independent sample surface properties, an estimate for the surface roughness and the curvature.

5.1. Surface Roughness

The granular structure of the phase distribution (see inset of Figure 5.4 (a) and (b)) is related to the surface roughness. Since we perform differential measurements, i.e. these phase distributions are compared to the ones retrieved using reference mirrors in both arms of the interferometer, we can estimate an upper limit for the surface roughness.

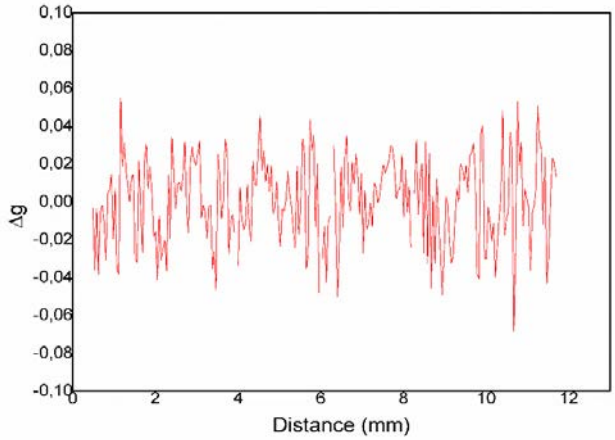

Figure 5.5 Phase distribution after high pass filtering.

The granular structure of the phase distribution $\Delta g(r)$ can be isolated by applying high-pass spatial filtering to the measured surface profile as shown in Figure 5.5. The high-pass spatial filter applied, cuts off spatial frequencies lower than f<3.7mm^{-1}. From the Root Mean Square (RMS) of the remaining values, Δg_{hf}, we get an upper estimate of the surface roughness, R_a, through equation 5.3:

$$R_a \leq \lambda \, RMS \, (\Delta g_{hf}) \qquad (5.3)$$

5.2. Curvature

The concentric annular formations in the phase distribution are related to the sample's surface curvature. The surface curvature can be estimated by fitting a low-pass filtered phase distribution to a parabola (Figure 5.6).

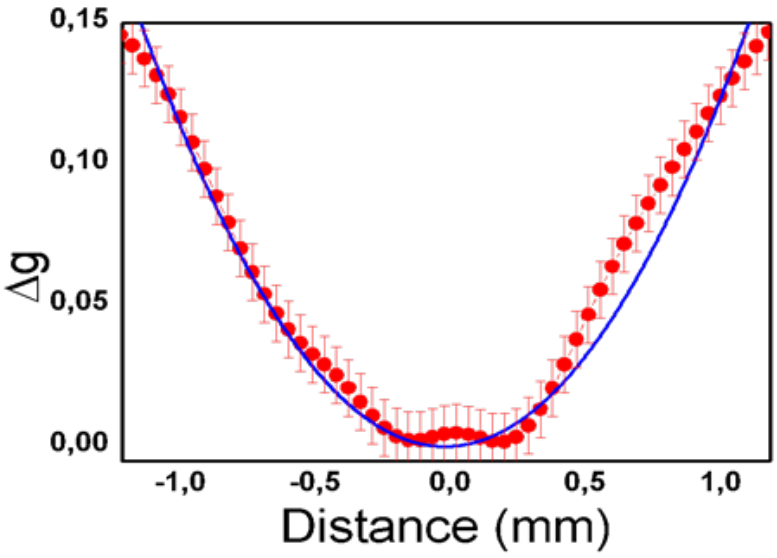

Figure 5.6 Phase distribution after low pass filter and the fitted parabola (blue line).

A spherical reflecting surface with radius of curvature R transforms a plane wave front to a spherical one after reflection, imprinting a parabolic phase distribution, described by equation (5.4):

$$\Delta g = -\frac{x^2}{2\,\lambda\,R} \qquad (5.4)$$

The radius of curvature R, can be estimated by fitting equation 5.4 to the measured phase distribution after the reference phase has been subtracted. This estimation gives a lower limit on the value of the surface curvature.

5.3. Angle Measurement and beam steering

Furthermore, the angle of each wedge was measured to compare with the specifications but also to be able to make pairs of wedges with practically identical angles.

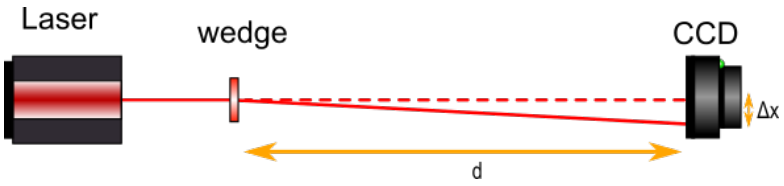

Figure 5.7 Schematic for measurement of wedge angle and measuring beam deviation.

The apparatus was simple but efficient (Figure 5.7). Using a (He-Ne) laser source and a CCD camera we were able to record the position of the beam with and without a wedge. Therefore, using the measured beam spatial deviation, Δx, at a specified distance d, and the refractive index n, the wedge angle, α, was calculated using the following equation 5.5:

$$\alpha = \frac{atan(\frac{\Delta x}{d})}{(n-1)} \qquad (5.5)$$

For experimenting with the beam steering technique, we positioned a pair of wedges in front of a laser beam that was directly pointing at a CCD camera (Imaging Source DMK 21 BU04), as in Figure 5.7. The wedges were rolled with the same translation stages and arms that will be used to align the optics on the breadboard. These translations stages have a sensitivity of 0.1μm and graduations every 1μm. One wedge was rolled and pictures were taken of the beam after 1mrad and 10mrad roll (Figure 5.8). For rolling 1mrad, the wedge must travel for about 6 μm since the radius of the wedge is 6mm.

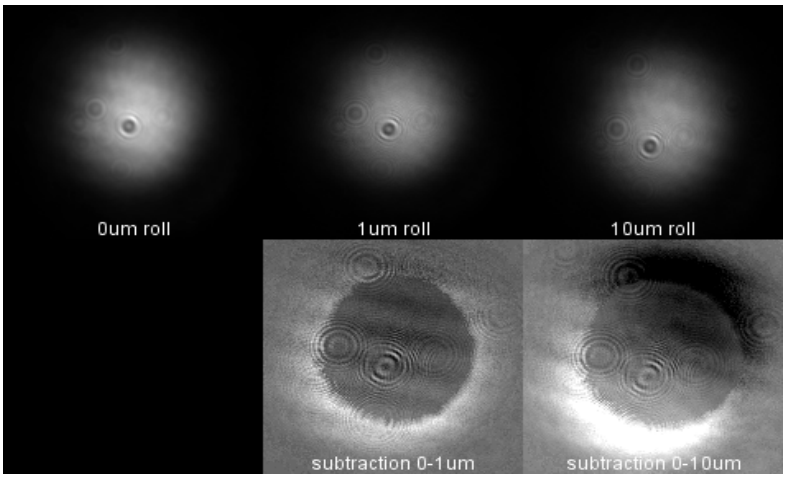

Figure 5.8 Beam spot before rolling a wedge, after 1mrad roll and 10mrad roll. Bottom, the beam displacement is visible when subtracting the intensity of each spot as white light.

The beam displacement, Δx, was measured at a distance d=50cm to increase the accuracy. The measured angle, Δφ, is calculated from:

$$\Delta\varphi = Arctan(\frac{\Delta x}{d}) \qquad (5.6)$$

The beam rotation for the equivalent wedge roll can be seen in the next table where it is compared with the predicted value using equation (3.5).

Wedge roll (mrad)	**Prediction (μrad)**	**Measurement (μrad)**
1	5.55	5.8± 0.3
10	55.5	56.1± 0.3

Table 5.1 Beam displacement in relation with wedge roll.

For displacing the beam, a similar procedure was followed for a glass plate. A laser beam was pointing directly at a CCD camera through a glass plate. A mirror mount was used to tilt the plate but since the plate only displaces the beam increasing the accuracy of the measurement was not possible by increasing the distance. For achieving 4mrad plate tilt, the mirror knob was turned half a circle and for 8mrad a full circle. The prediction from equation (3.6) and the results of the measurements are shown in Table 5.2:

Plate tilt (mrad)	Prediction (μm)	Measurement (μm)
4	3.8	5± 0.5
8	7.7	10.5± 0.5

Table 5.2 Beam displacement in relation with plate tilt.

The values for rotating the mirror knob where chosen as they are easily achieved with the knob and quantified. Nevertheless, since it is quite feasible to rotate a knob for 5°, the tilt of the plate would then be 100μrad which would produce approximately 100nm of displacement and that would be closer to the actual accuracy. It is clear that alignment precision of the beam is in the order of at least few micrometers and micro radians. Even without pushing to the limit of the equipment used, the displacement of the beam is equivalent of other methods and can easily exceed the sensitivity of other aligning systems.

5.4. Focal length measurement

Lastly, a plano-convex focusing lens with f=500mm was measured to validate the procedure and the apparatus used. It should be noted that the imaging system, that was used, was not an afocal system. An afocal system does not alter the divergence of a beam and it created when the distance, d, between two optics is the sum of the focal lengths of the two optics. It is more accurate for measurements, as it does not transform the wave, meaning curvature is not added by the system. While a typical imaging system adds curvature depending on the distances chosen.

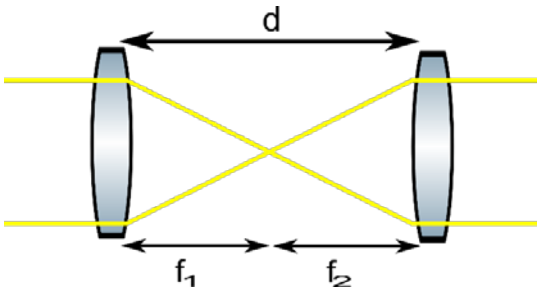

Figure 5.9 Afocal optical system of two lenses. The focal length is f1 and f2 for the 1st and 2nd lens respectively. The distance between the lenses is the sum of the focal lengths.

Due to specific constraints we could not implement an afocal system in our case. More specifically, each optic element produced two reflections when illuminated, one for each surface. In order to filter out one of them and acquire the interferogram, enough spatial separation was needed amongst the two reflections. The use of an afocal optical system does not favor this filtering, however, when moving the camera lens further away from the imaging lens, the two reflections were spatially separated with the drawback of adding optical power to the imaging system (Figure 5.10). This resulted in adding an extra curvature to the wave fronts that reached the sensors that needs to be taken into account in the calculations.

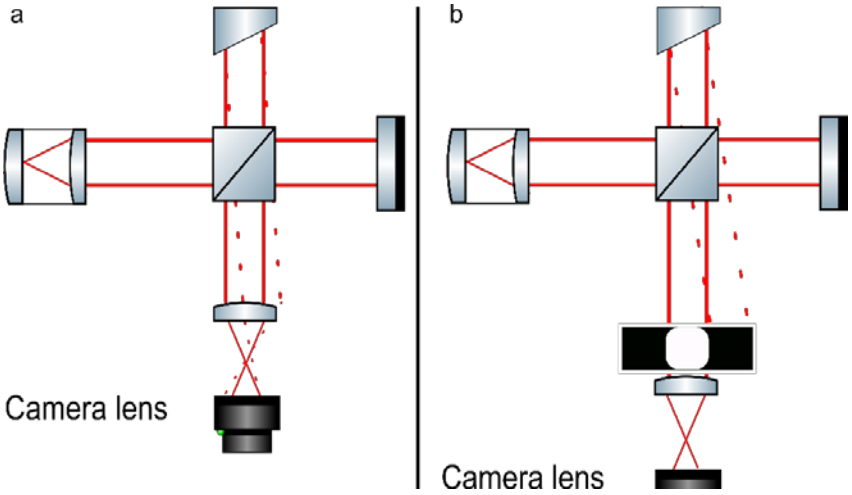

Figure 5.10 In picture a shows the afocal system with the two reflections from the wedged prim where spatial separation is not enough for filtering. In picture b, the camera lens has been providing space for the filtering.

Using ray matrix theory, the curvature incident on the CCD sensor can be calculated in relation with the curvature of the tested optic. The q factor can fully describe a beam, which is defined using the curvature, R, of the wave, the beam waist, w, and the wavelength λ as seen in equation 5.7 [37].

$$\frac{1}{q} = \frac{1}{R} - i\frac{\lambda}{\pi w^2} \qquad (5.7)$$

First of all, it is assumed that the beam waist is located at the end of telescope and therefore R→∞. Then, the factor q_{in} of the incoming beam is described by equation 5.8:

$$q_{in} = i\,\pi\,\frac{w^2}{\lambda} \qquad (5.8)$$

To estimate the ray matrix of the system all distances have been measured from the principal planes of the equivalent optics (Figure 5.11).

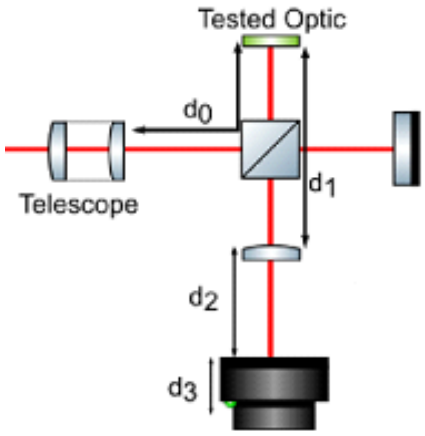

Figure 5.11 Distances measured for the matrix taking into account the refractive index where it is necessary.

We can use ray matrix theory [38] to describe our optical system where the matrix of the system is given by equation 5.9:

$$M = \begin{pmatrix} 1 & d_3 \\ 0 & 1 \end{pmatrix}\begin{pmatrix} 1 & 0 \\ P_{cam} & 1 \end{pmatrix}\begin{pmatrix} 1 & d_2 \\ 0 & 1 \end{pmatrix}\begin{pmatrix} 1 & 0 \\ P_{lens} & 1 \end{pmatrix}\begin{pmatrix} 1 & d_1 \\ 0 & 1 \end{pmatrix}\begin{pmatrix} 1 & 0 \\ P_{test} & 1 \end{pmatrix}\begin{pmatrix} 1 & d_0 \\ 0 & 1 \end{pmatrix} = \begin{pmatrix} A & B \\ C & D \end{pmatrix} \quad (5.9)$$

where P_{cam}, P_{lens} and P_{test} is the optical power of the Pentax lens system, the imaging lens and the tested optic respectively. The quantities, that are needed for calculations, are shown in Table 5.1 and R is the curvature of the optic element under test.

Normalized Distance		Optical Power	
d0	210 mm	P_{cam}	-62.5 m^{-1}
d1	95 mm	P_{lens}	-10 m^{-1}
d2	128 mm	P_{test}	$-\frac{2}{R}$
d3	16 mm		
Waist of the beam (w)			0.95mm

Table 5.3 Measured quantities.

The matrix takes the following form when the values are applied:

$$M = \begin{pmatrix} -0.16 + \frac{0.0016}{R} & 0.0008 + 0.21(-0.16 + \frac{0.0016}{R}) \\ 7.7 - \frac{12.6}{R} & -6.3 + 0.21(7.7 - \frac{12.6}{R}) \end{pmatrix} \quad (5.10)$$

Then the q factor of the beam incident on the CCD sensor is described by equation 5.11 [37]:

$$q_{out} = \frac{A\, q_{in} + B}{C\, q_{in} + D} \quad (5.11)$$

The real part of the inverse q_{out} factor is the curvature of the incident beam on the CCD sensor, R_{out} as shown in equation 5.12:

$$R_{out} = Re\left[\frac{1}{q_{out}}\right] \quad (5.12)$$

By combining equations 5.10, 5.11, 5.12, the numeric relation between the curvature R_{out} and the incident curvature, R, can be calculated used for each optic element.

$$R_{out} = \frac{-2.1\ 10^{-3} + (0.42 - 21R)R}{0.016 + R(-1.66 + R)}\ 10^{-3} \quad (5.13)$$

Furthermore, since the measurement is differential, the reference curvature should be subtracted from the corrected curvature. Since two parabolas are subtracted, the actual curvature of the tested element, R_{opt}, is given by equation (5.14):

$$\frac{1}{R_{opt}} = \frac{1}{R_{ref}} - \frac{1}{R} \quad (5.14)$$

where R_{ref} is the reference curvature of the mirrors which was measured in the first step of the experiment.

For the plano-convex lens which had f=500mm and therefore R=290mm, the radius of curvature was comparatively measured using the aforementioned system and after adjusting the distance between imaging lens and camera lens, to an afocal system.

Moreover, the same lens was measured by removing all imaging optics from the interferometer. In this case the effect of the beam propagation should be taken into account in our calculations. The values measured with each technique are shown in Table 5.4.

	R_{lens} Value (mm)	Error (mm)
Nominal value	290	-
Imaging system	350	±30
Afocal system	320	±30
Free propagation	370	±30

Table 5.4 Focal length of a lens measurements with different optical systems.

The comparison of the three optical set ups indicates that the afocal system is the more accurate. However, without optics the wave front that is analyzed is not the one that is reflected by the optic under test, since the wave front has changed due to the propagation. Furthermore, an imaging system introduces errors that are difficult to evaluate with precision. Taking all this into consideration, it is safe to conclude that an afocal system is the most efficient system to use. Nevertheless, in some cases where there are other constraints like in our case, an imaging system can be used with sufficient accuracy.

5.5. Results

Several wedges and glass plates were measured using the aforementioned technique. The results of the measurements for the wedges can be seen in Table 4.3 and in Table 4.4 for the glass plates. Wedges were tested from two suppliers; Thorlabs (TH1-4) and Casix (CA1,3,8).

Wedge	Measured Curvature (R_{opt} in m)	Measured Roughness (λ=633nm)	Specifications	wedge angle (Arcmin)	Specifications (Arcmin)
TH1	12.1±0.1	<λ/12	< λ/10	34.2±1.2	30±10
TH2	13.3±0.1	<λ/11		30.6±1.2	
TH3	14.2±0.1	<λ/11		30.1±1.2	
TH4	14.7±0.1	<λ/14		30.6±1.2	
CA1	11.4±0.1	<λ/14		35.4±1.2	
CA3	10.9±0.1	<λ/15		34.8±1.2	
CA8	11.2±0.1	<λ/14		34.8±1.2	

Table 4.3 Measured values for wedged prisms.

Glass Plate	Measured Curvature (R_{opt} in m)	Roughness (λ=633nm)	Specifications
EKSPLA IV	20.8±0.1	<λ/13	< λ/10
EKSPLA VI	21.4±0.1	<λ/14	
EKSPLA VII	20.6±0.1	<λ/10	
EKSPLA VIII	21.7±0.1	<λ/10	

Table 4.4 Measured values for glass plates.

In view of the previous results, we have paired wedges with almost identical angles as follows in Table 4.5:

30arcmin	60arcmin
TH2-TH4	CA10-CA11
TH1-CA1	CA12-CA13
CA3-CA8	
TH3-CA9	

Table 4.5 List of wedge pairs.

All optics that were used were found in compliance with specifications. Therefore, they are deemed eligible for use in optical set ups.

6. Optical Breadboards

Building a novel optical breadboard is a very challenging procedure. To isolate and identify the problems that may occur, different techniques should be independently tested. Therefore, aluminum and simple glass mock-ups were build, before the final zerodur breadboard. In the aluminum mock-up, the alignment technique was evaluated using commercial collimators and without the use of translation stages or mirror mounts. A breadboard consisting of two couplers a pair of wedges and a plate was assembled. All the mounting blocks were prepared in FORTH-IESL workshop in close relation to the final Zerodur components. Using the wedges and the glass plate, we tried to maximize the transmitted optical power. This was the first step to confirm the alignment technique.

Then in a glass mock-up more precise alignment was performed and the gluing steps were investigated to determine the exact procedure that should be followed to build the final breadboard. Instead of aligning by hand, translation stages and mirror mounts were added to improve the accuracy of the alignment process. Moreover, valuable training was obtained by applying UV adhesive on glass blocks. Glass blocks that are cheap and easily replaceable, permitted us to experiment with the process and gradually discover all the necessary steps to format the optimum technique.

6.1. Aluminum breadboard

The first metallic mock-up aimed to test the alignment procedure. It consisted of the aluminum couplers, an aluminum mount with Teflon holders for the wedges and aluminum holders for the glass plate (Figure 6.1). The aluminum couplers were rectangular blocks prepared in the FORTH-IESL workshop with a hole in the middle where a fiber collimator would be placed. In order to have a stable assembly, one more threaded hole was drilled vertically. After horizontally inserting a fiber collimator, the assembly was tightened from the vertical side. Two such assemblies were then glued on an aluminum plate facing each other.

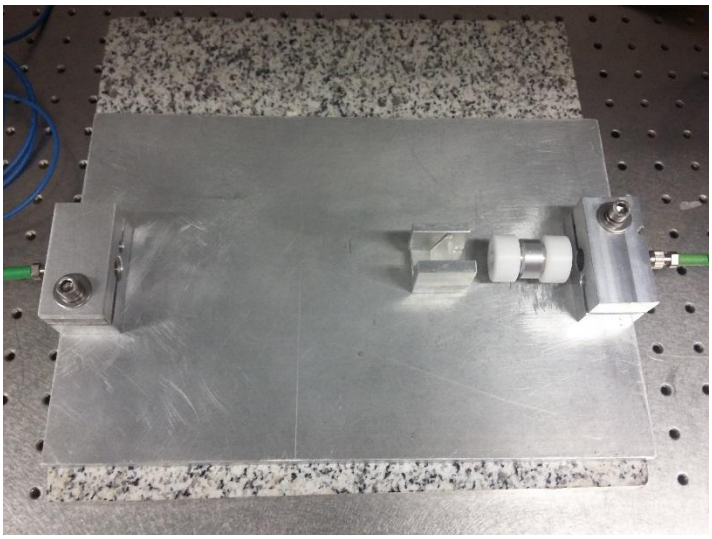

Figure 6.1 First aluminum breadboard.

The mount for the wedges is a cylinder where two wedges will be placed, one from each side (Figure 6.2). The wedges are pressed on the aluminum cylinder using Teflon cylinders with larger diameter. To avoid scratching the wedges, plastic o-rings are placed between the wedged prism and the aluminum mount. The prisms can be rotated easily by hand using the Teflon cylinders and therefore adjust the beam alignment.

Figure 6.2 Wedge mount and aluminum holders for the glass plate.

The holders for the glass plate are one orthogonal block and one Γ-shaped block. Together they form a π-shaped assembly where the glass block is placed. Then, the holders are glued together while gently pressing them. The friction between the glass plate and the holders should be just enough to hold the plate at any angle. The tilt of the glass plate is performed by hand to adjust the pitch, while for the yaw the entire π-assembly is rotated.

With the described steps, the aluminum breadboard was assembled and aligned. Without the corrective optics there was not any light coupled from one fiber into the other. After aligning the system, the output optical power was increased significantly. Therefore, the alignment method produced positive results but should be improved as aligning by hand is not optimal.

The second version of the metallic mock-up has improved designs of all components (Figure 6.3). Since on the final design bare ferrules would be place inside the zerodur couplers, the same principle is applied to the second version of mock-up. The metallic couplers are simple cubes with one hole which has different diameter at opposing sides.

Figure 6.3 Metallic mock-up version 2.

At the front, the hole has a thread for a mounted aspheric lens (Thorlabs C230TMD-B with f=4.51mm) while in the back side the hole with a smaller diameter will support the bare ferrule of a single mode fiber (Thorlabs SMPF106) (Figure 6.4). To collimate the beam, the ferrule is moved inside the hole longitudinally.

Figure 6.4 Front and back view of the metallic coupler.

The wedge mounts are now tubes with outer diameter larger than that of the wedge, d_{outer}=15mm, while the inside diameter, d_{inner}=8mm, provides enough space for the beam to propagate (Figure 6.5). The wedged prism is glued on the ring using LOCTITE 401 instant adhesive. The wedge holders roll on the metallic breadboard aligning the beam and then fixed in position by a set of cubes which are glued to the breadboard and to the wedge holders.

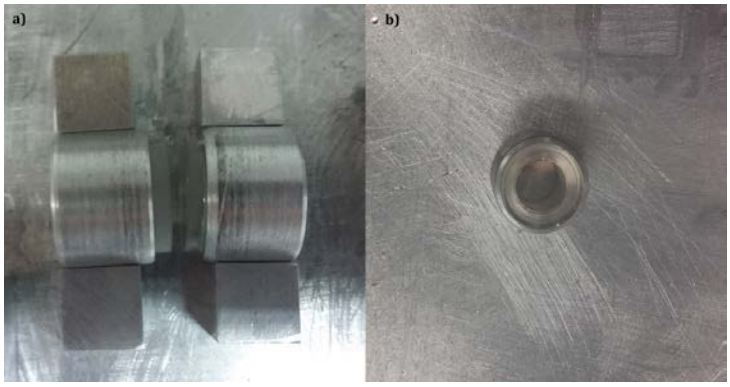

Figure 6.5 Wedge mounts with the prisms being in proximity and held in position by a set of cubes(a), and front view(b).

The glass plate is glued to two vertical blocks without the use of a bottom surface. Since the wedge holders are now glued on the breadboard, the height of the glass plate is also reduced (Figure 6.6).

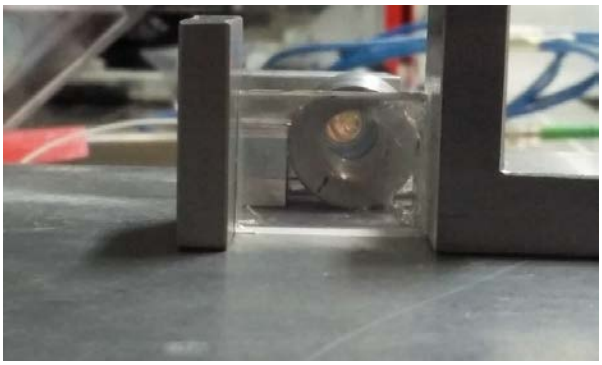

Figure 6.6 Glass plate glued to two vertical surfaces in front of the wedge holders.

The alignment was performed again by hand optimizing but the accuracy was not enough to achieve high optical power transmittance. The metallic mock-up successfully demonstrated the validity of the alignment technique and the next steps were to increase the accuracy of the alignment and test the gluing procedure.

6.2. Glass breadboard

Soda lime glass was used to manufacture a small plate and blocks to replace the metallic parts. The wedge holders were not replaced by glass tube because manufacturing proved to be complicated and costly for a mock-up (Figure 6.7). The same approach was applied to glass couplers and since the alignment and the bonding sequence of the optics are the investigated parameters, commercially available fiber couplers are used to facilitate the integration of the mock-up.

Figure 6.7 Glass breadboard made of soda lime glass.

In order to increase the accuracy of the alignment, translation stages were used for rolling the wedges and a mirror mount for tilting the glass plate. Two xyz translation stages (Newport M-562) were positioned bilateral of the breadboard. On each translation stage a long metallic arm is screwed and it is lowered until it presses down the wedged prisms. When moving the translation stages, the wedges are forced to roll through friction (Figure 6.8). After aligning the wedges and gluing them to the blocks the arm is lifted and removed easily.

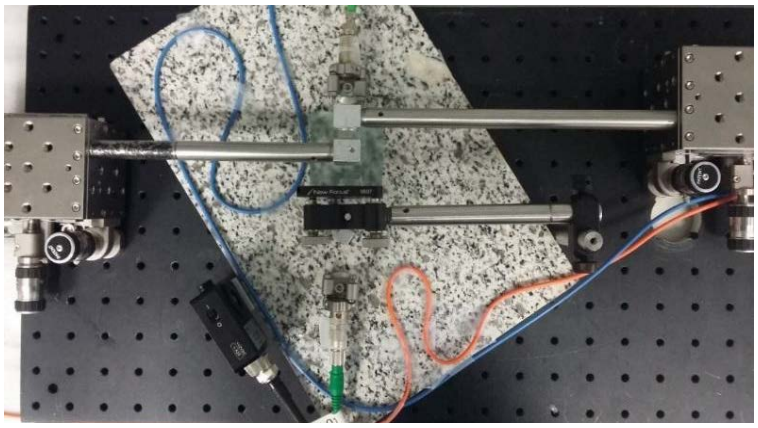

Figure 6.8 Aligning a glass breadboard with two translation stages and a mirror mount.

Furthermore, the glass plate is attached to a mirror mount (New focus 9807) to increase the accuracy of the tilt. The idea is to attach the glass plate to the mirror mount using thermoplastic glue which allows us to detach the plate with minimum force. However, the interface between metal and glass does not adhere firmly when using Crystalbond. To bypass this obstacle, a soda-lime block is glued to the mirror mount using LOCTITE 401 and the glass plate is glued to the glass block using Crystalbond 509 (Figure 6.9). With this procedure, easy detachment and firm adhesion is achieved, for more details on the procedure please refer to 7.3 Alignment Setup.

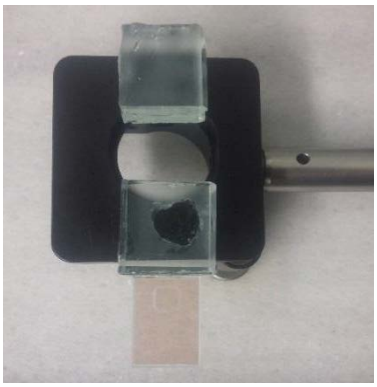

Figure 6.9 Glass plate attached to glass block which is glued on a mirror mount.

A rough alignment is performed by hand and then optimized using the translation stages and the knobs of the mirror mount. The translation stages have 1μm resolution which corresponds to 0.3 mrad roll for the prisms since the diameter of the prisms is 6.3mm. The sensitivity of this mirror mount is 19μrad tilt if the rotation knob is adjusted by 1^{o}, which results in 19nm beam displacement sensitivity.

7. Final Zerodur breadboard

The zerodur components were manufactured by Microbas Precision AB in Sweden. The design of each component is unique and facilitates the integration of the entire system (Figure 7.1).

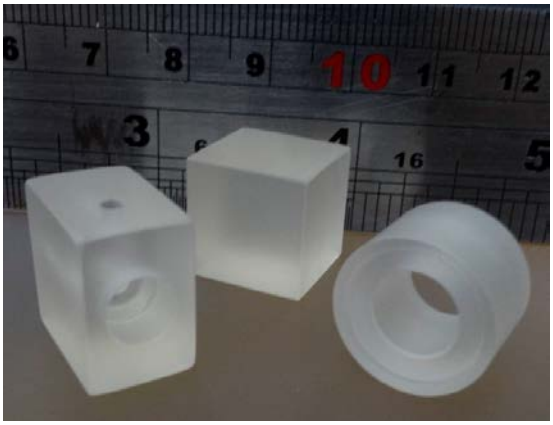

Figure 7.1 Zerodur components. From left to right: Zerodur coupler, block and wedge holder.

Before integrating the Zerodur breadboard, two sub components should be assembled. First and most crucial, the zerodur fiber coupler is assembled, which is composed by a Zerodur coupler, an optical fiber and a lens. Then, a wedged prism is attached to a wedge holder and finally all the optics are placed on the Zerodur breadboard.

7.1. Zerodur fiber coupler

The first step for assembling the Zerodur coupler is surface preparation. Zerodur couplers are cleaned inside an isopropanol bath under ultrasound for 30 minutes. Then, the adhesive, Norland Optical Adhesive 61 (NOA61), is applied to the inner rim of the Zerodur coupler where the aspheric lens (Thorlabs 355230-B) will be placed. In order to produce a glue layer with height less than 10μm, a volume of 0.6μL is placed on a disk with a precision micropipette, Gilson Microman precision microliter pipette (Figure 7.2).

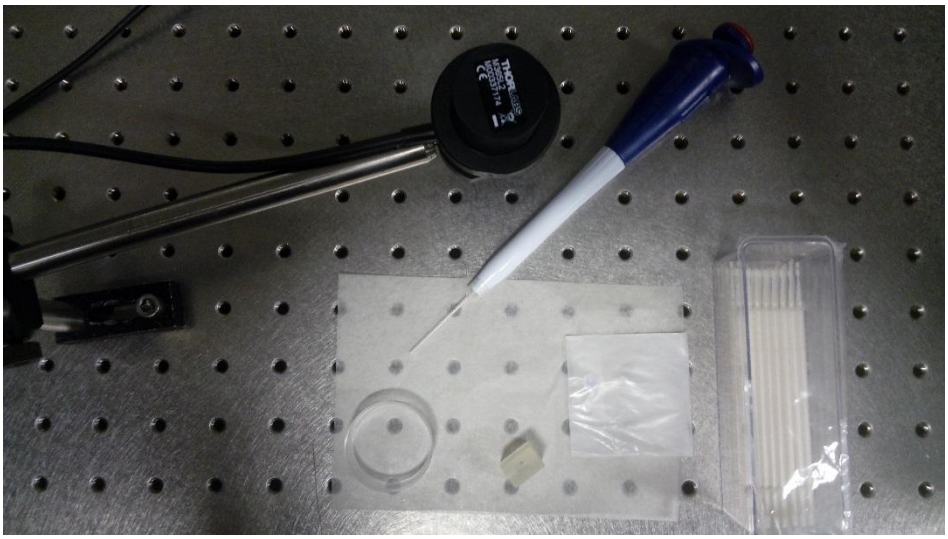

Figure 7.2 Coupler assembly equipment. Visible are the UV lamp, the micropipette, disk to deposit the adhesive, a Zerodur coupler and glue micro brushes.

Using then glue micro brushes, this amount of adhesive is spread along the rim of the couplers (Figure 7.3).

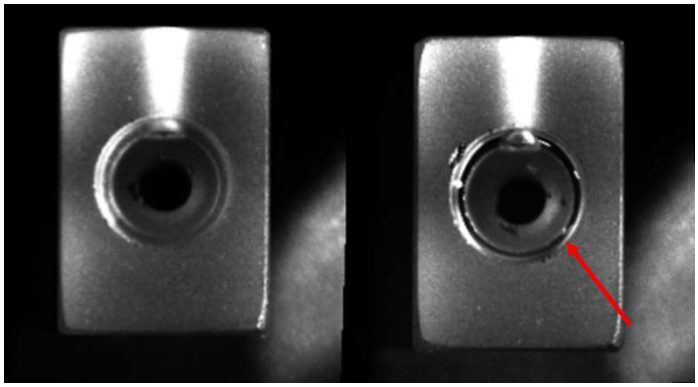

Figure 7.3 Zerodur coupler before applying NOA61, left, and after applying the glue on the rim, right. The ring appearing as black in the photo is the applied NOA61.

The aspheric lens is then positioned inside the coupler and on top of the applied glue and pushed into place. The assembly is ready for curing which is performed using the Tholarbs UV LED (model M365L2) (Figure 7.4) at an approximate distance between the lens and the UV LED of d=10cm. The UV LED produces a maximum power of 360mW at

λ=365nm when driven with 700mA which is the recommended current of operation. The current is supplied by an LED driver (THORLABS LED1B) which can ramp the output power to the maximum using a knob with 6 graduations. The power is gradually ramped up to maximum, spending 5 min per graduation until the last, where time spent is increased to 60 min to ensure complete and strong bonding.

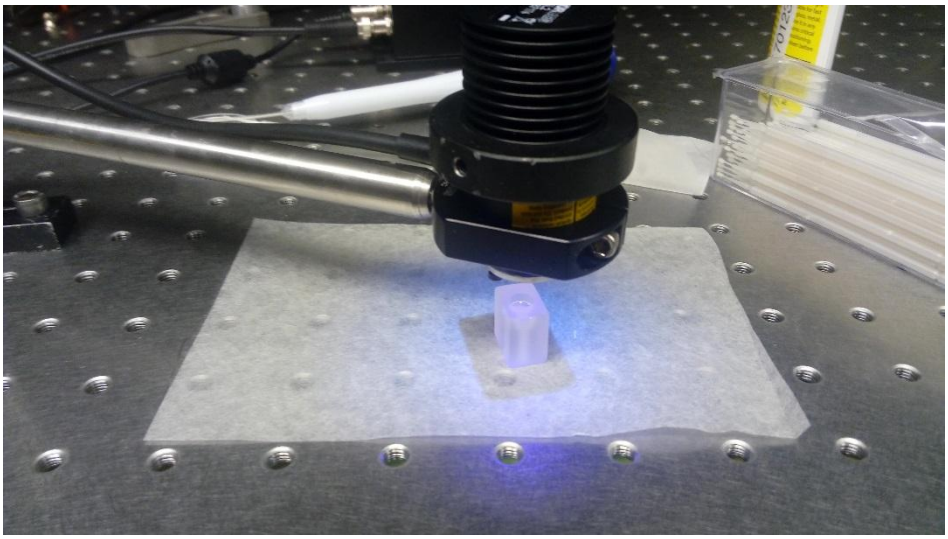

Figure 7.4 Curing the coupler-lens assembly.

The next step is to collimate the coupler with a fiber. The laser source for every laser beam produced, henceforth, is a standard laser diode at λ=780nm. The Zerodur coupler is firstly placed on a glass plate, free standing. This allows curing light to illuminate from almost all directions. Simultaneously, the bare ferrule end of a polarization maintaining (PM) fiber is positioned by a 6 degree of freedom mount assembly (Figure 7.5). The assembly consists of a translation mount (Newport M-562 series) for xyz movement, a mirror mount (Thorlabs KC1 cage mount) for aligning the ferrule with the coupler and a rotation mount (Thorlabs CRM1 cage rotation mount) for fixing the polarization.

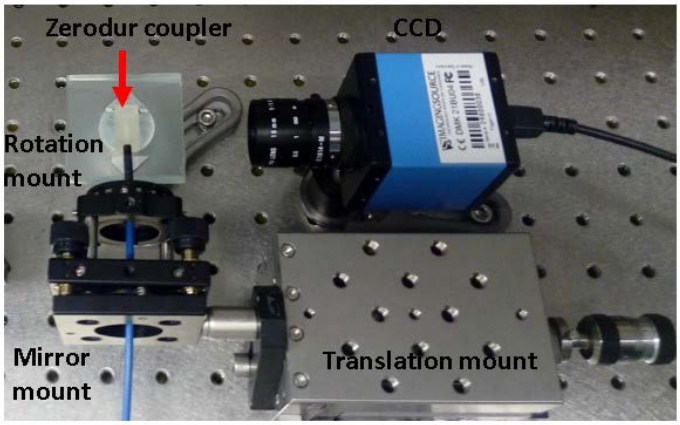

Figure 7.5 Collimation setup consisting of a translation, a mirror and a rotation mount. The fiber ferrule is inside the Zerodur coupler.

The fiber used is a standard Thorlabs PM780-HP fiber with FC/APC connector on one side and bare ceramic ferrule on the other side (Figure 7.6). The bare ceramic ferrule end will be inserted in the Zerodur coupler to assemble the component.

Figure 7.6 Thorlabs PM780-HP fiber with FC/APC connector on right side and bare ceramic ferrule on left side.

First, the ferrule is aligned in respect to the coupler using the mirror mount shown in Figure 7.5. Afterwards, the polarization axis of the PM fiber is fixed in respect to the optical table. Linear polarization is coupled into the fiber with the axis parallel to one of the fiber axis and the output is measured after a polarizing beam splitter (Thorlabs PBS252).

Using a rotation mount, the ferrule of the PM fiber is rotated until the transmitted power after the PBS is minimized. We have achieved extinction ratio 0.8% when the specification of the PBS used is 0.1%. This means that the axis of the PM fiber is aligned to the PBS.

Before collimating the beam, the adhesive is applied on the ferrule. Using the translation stage, the ferrule is moved backwards to exit from the coupler without rotating the ferrule. A volume of 0.6μL NOA61 is applied on the ferrule using a micro brush and the ferrule is re-inserted into the coupler.

The next step is the collimation of the beam. The waist of the beam is placed at a position which is calculated based on the components of the breadboard in order to have the optimum mode coupling. This is achieved by minimizing the diameter of the beam at a calculated distance. To achieve the minimum diameter, the ferrule is moved longitudinally in respect to the lens (Figure 7.7). During this process, the movement of the ferrule is inspected by cameras, from to orthogonal views to ensure that it is well aligned with the Zerodur coupler and there is no significant drag or hysteresis.

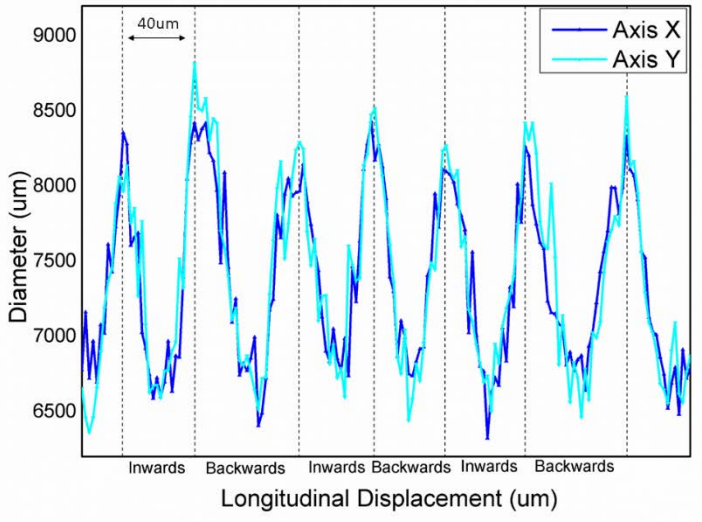

Figure 7.7 Beam diameter while moving the ferrule continuously back and forth, around the position with the minimum diameter.

The collimation is monitored and recorded using a beam profiler (Ophir Photonics NS2- Ge/9/5). Moreover, we are using a translation stage (Newport M-562 series) to move the ferrule to the optimum position with high precision. The translation stages have 1μm

resolution and the beam profiler resolution is a few micrometers, depending on the wavelength. Therefore, we can position the ferrule to the optimum position with an accuracy of 1-2μm which produces an error on the CE less than 1%.

After achieving the minimum position, the adhesive is cured using the UV LED. The curing distance is chosen again to be d=10cm but since the adhesive is inside the Zerodur coupler and the curing light needs to pass through Zerodur, the curing time calculation must take into account the transmissivity of Zerodur at λ=365nm. Zerodur has approximately 8 times less transmissivity than glass, which increases the curing time by a factor of 8. Therefore, each coupler is cured for approximately 8 hours. During curing, the beam diameter is monitored with the beam profiler and compared to the theoretical value at that distance (Figure 7.8). The diameters measured were insensitive to the procedure and exceeded the predicted stability. As it is evident from Figure 7.8, the deviation from the theoretical value was 2% for the y axis and 1% for the x axis.

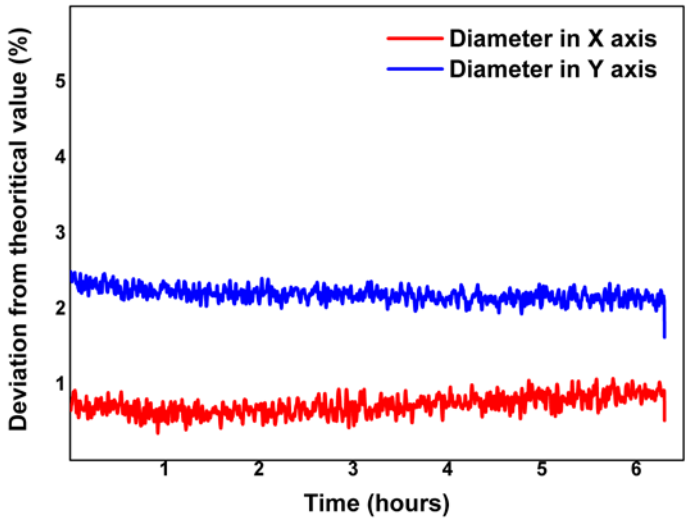

Figure 7.8. Beam deviation form theoretical value during curing.

After curing, the beam profile is measured to compare with the one before curing. The diameters before and after curing exhibit minor differences of the order of 1-2% which are within measurement error (Figure 7.9).

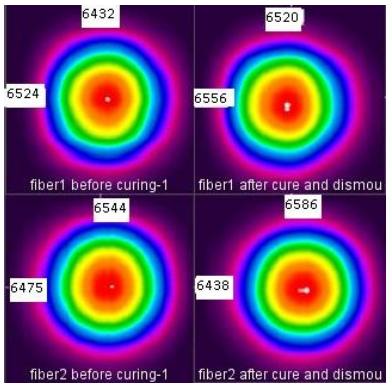

Figure 7.9 Beam profiles of the first two fibers glued inside Zerodur couplers.

The coupler assembly is now complete so it can be positioned on the breadboard. The produced assembly has the beam quality and beam characteristics that were targeted. It is a robust monolithic device with a simple design that can be built efficiently and reproducibly, while errors are limited to the order of 1% in beam diameter.

7.2. Wedge holder assembly

The wedge holder assembly starts by cleaning the surface of the Zerodur component. It is placed inside an isopropanol bath and cleaned with ultrasounds for 30 minutes. Then, 0.8μL of NOA61 are applied to the inside ring of the wedge holder using again a micropipette and micro brushes (Figure 7.10).

Figure 7.10 Wedge holder just before applying the adhesive.

Afterwards, the wedged prism is positioned inside the wedge holder and the adhesive is cured from a distance of d=10cm by gradually ramping up LED power to the maximum, spending 5 min per graduation, until the last, where time spent is increased to 60 minutes to ensure once again complete and strong bonding (Figure 7.11).

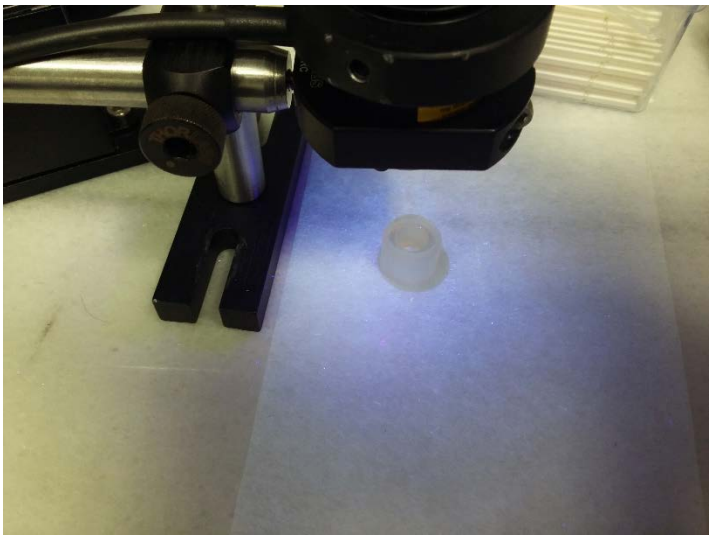

Figure 7.11 Zerodur wedge holder curing.

The assembly of the wedge holder is complete and can now be placed on the OBST breadboard.

7.3. Alignment Setup

Initial alignment is performed by placing the two assembled Zerodur couplers opposite of each other at a separation distance of L=175mm. Beneath each coupler we apply a volume of 2μL of NOA61 using the micro pipette. A mirror mount with a homemade adapter is used to hold the fiber end of the Zerodur coupler. This way, the couplers are held above the Zerodur breadboard at an approximate distance of h=1mm. Using a spacer, we position the couplers with an accuracy <100um relative to the end of the Zerodur breadboard. Then, a laser source is connected to both couplers and by gently moving the couplers by hand, we move the counter propagating beams until they visually coincide. When the beams are as

close as possible, the couplers are pressed firmly vertically downwards using arms that are screwed on translation stages. Now, the couplers are in contact with the breadboard and we can see the adhesive spread and cover the whole surface below the coupler.

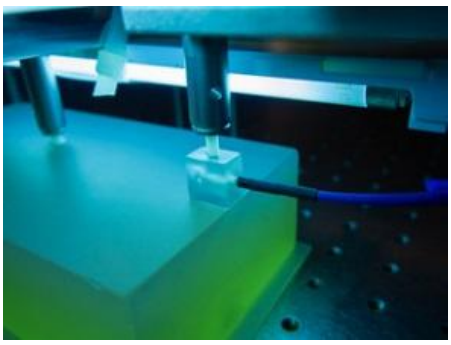

Figure 7.12 Zerodur coupler pressed down while curing the adhesive.

At this point the adhesive below the couplers is cured (Figure 7.12). The thickness of Zerodur that needs to be traversed by the light is increased in regard to the assembly of the coupler. Therefore, curing time should be at least 72 hours due to the Zerodur transmissivity.

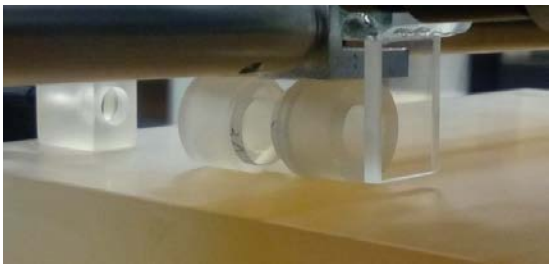

Figure 7.13 Corrective optics in place for aligning. The two wedge holders are placed such as to have the wedged prisms opposite to each other.

Next, the corrective optics are placed on the breadboard. The wedge holders are positioned in front of the transmitter, with the wedged prisms facing each other (Figure 7.13) in order to minimize the separation distance between the wedged prisms. The prisms are rolled using an extension rod, which are attached to translation stages to align the beam, as shown in Figure 7.14.

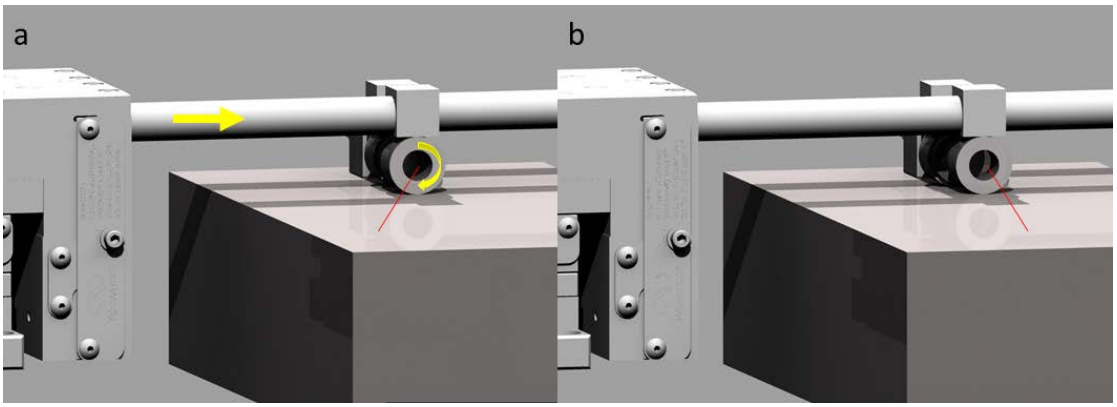

Figure 7.14 Beam alignment with the wedges. The yellow arrows in the left picture denote the movement of the extension rod and the roll of the wedge. In b, the beam angle has changed due to the roll.

The translation stages are positioned in opposite sides of the breadboard. Two metallic arms are screwed on the translation stages which also press the wedge holders firmly downwards. The wedges are roughly pre-aligned by hand since the initial alignment requires large rotations of the wedges.

The glass plate is attached to a mirror mount (New Focus 9882) and positioned in the desired place with the help of an optical post assembly (Thorlabs TR75/M posts and Thorlabs 90/M clamp). To temporarily attach the glass plate we use Crystalbond 509 thermoplastic adhesive which can be easily removed after aligning. Because Crystalbond exhibits the highest bond strength between glass-glass interfaces, we use a glass block to attach the glass plate to the mirror mount. The glass block is glued on the mirror mount using Loctite 401 cyanoacrylic adhesive. Then, at the bottom surface of the glass block we apply thermoplastic adhesive Crystalbond 509 which is heated and attached to the top surface of the glass plate (Figure 7.15). A heat gun (Steinel HG 2310 set to 100^{o}C at minimum air fan speed) is used to heat the Crystalbond for 1 minute. First, the glass plate roll is aligned to the breadboard using the Zerodur block that will be used later to fix the position of the plate. The block is pressed on the side of the plate and Crystalbond is heated. The side of the plate is now perpendicular to the breadboard. Then, the pitch and yaw of the glass plate are roughly aligned, by hand turning the mirror mount on its post, while precise alignment is performed using the mirror mount adjustment knobs.

Figure 7.15 The glass plated attached to the glass block. A drop of Loctite401 in the middle of the glass block is also clearly visible.

After positioning all the corrective optics on the breadboard, we use the translation stages and the mirror mount to align the system to maximize the transmitted optical power (Figure 7.16). The power is monitored using a Si photodiode (ThorlabsFDS1010) and an oscilloscope. With this setup we have a precision in tuning the angle of a few μrads and position a few μm. This way we can tune the maximum transmitted power with precision of the order of 0.5%.

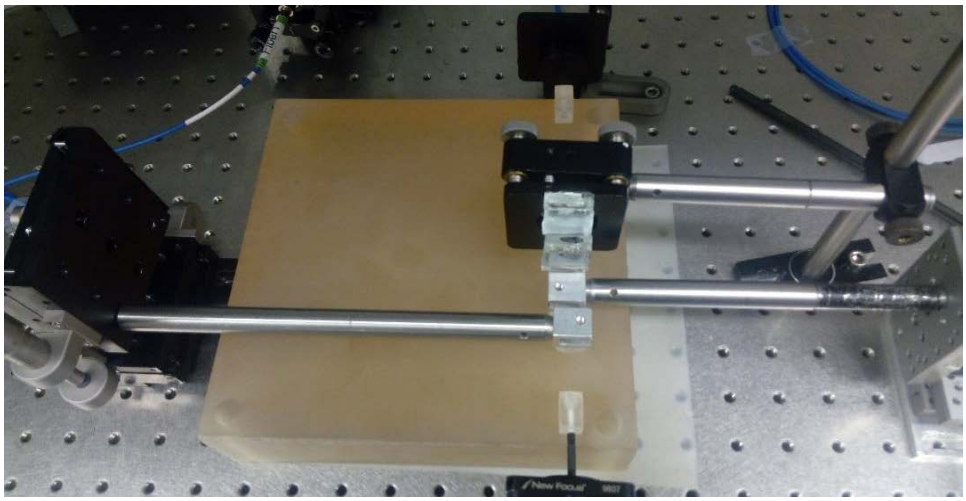

Figure 7.16 Complete alignment setup.

7.4. Adhesion

After aligning, the optics should be glued and fixed in position. For each wedge holder two blocks are used. Each block will adhere to the breadboard and to a wedge holder. Therefore, two adjacent sides of Zerodur blocks are covered with 2μL NOA61. Two Zerodur blocks are positioned on the sides of the wedge holders (Figure 7.17) and brought into contact with the holder. The transmitted power should remain the same during this process.

Figure 7.17 Zerodur blocks on the sides of wedge holders. The arms have been momentarily removed to increase the visibility of the Zerodur parts.

The glass plate is also fixed in position using two more Zerodur cubes. Again 2μL of NOA61 are used on two sides and the cubes are positioned on the sides of the plate (Figure 7.18). The cubes must be in contact with the glass plate without however, changing the transmitted power. Importantly, the glass plate is still attached to the mirror mount.

Figure 7.18 Zerodur blocks holding in position the glass plate.

The breadboard is now ready for curing the adhesive. The adhesive should be cured for at least 72 hours to ensure that curing has been complete. The translation stages can now be removed from the wedge holders and the transmitted power should not be affected. The glass plate is then detached from the mirror mount, by heating the thermoplastic glue to about 120^{o}C for 2 minutes' time using a commercial heat gun set at minimum air flow. The glue is flowing at this temperature and separation is achievable without reducing the transmitted power.

Figure 7.19 Assembled Zerodur breadboard. Visible are the pair of wedges with their holding blocks, a glass plate with a holding block and two zerodur fiber couplers facing each other.

The Zerodur breadboard is now assembled and can be tested (Figure 7.19). It is evident from the picture that the two wedge holders are dislocated relative to each other and the glass plate is in a rather large angle. The reason is that when placing the two Zerodur couplers, the accuracy used was minimum, as the optics would compensate for the misalignment.

8. Breadboard testing

The most crucial factor to assess the performance of the assembled Zerodur breadboard will be the measurement of the CE. The goal is to retain a high CE long term through thermal cycling and vibration testing. Since this assembly targets space mission it should be able to withstand some simple mechanical shocks and operate in a range of temperatures 10-40^{o}C.

8.1. Coupling Efficiency measurement

The optical system is outlined in Figure 8.1. It consists of three parts: The Transmitter and Receiver modules and the OBST alignment optics.

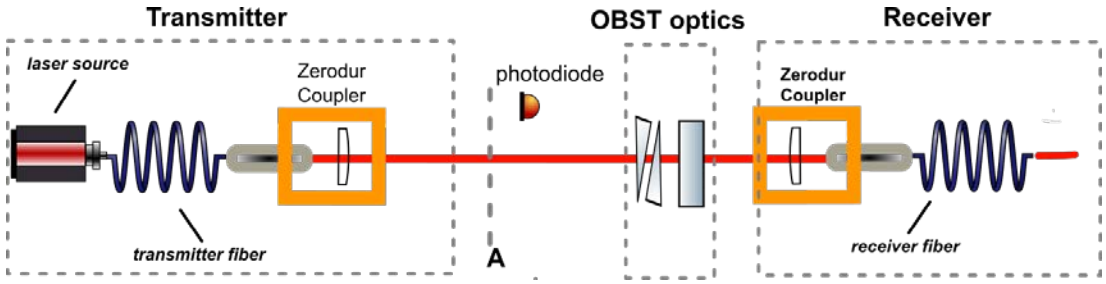

Figure 8.1 Optical system. Transmitter and Receiver modules are optically connected using OBST optics. (A) denotes the exit of the Transmitter module.

The CE is the percentage of the input optical power transmitted through the system:

$$CE = \frac{P_{tr}}{P_{in}} \qquad (8.1)$$

where P_{in} is the input optical power measured at the exit of the transmitter module (plane A in Figure 8.1) and P_{tr} is the output optical power measured at the exit of the Receiver fiber. These two quantities will be measured with the same Si photodiode (Thorlabs FDS1010). The photodiode was connected to a multifunction I/O device (NI 6229, 16 bit, 250kS/s),

through an electrical circuitry, as the one shown in Figure 8.2. In this configuration the measured signal, S_i, is proportional to the optical power, P. We have used a resistance R=33kΩ, and a capacitor C=220nF which attribute to our system a bandwidth fb=22Hz and signal to noise ratio, SNR=30dB.

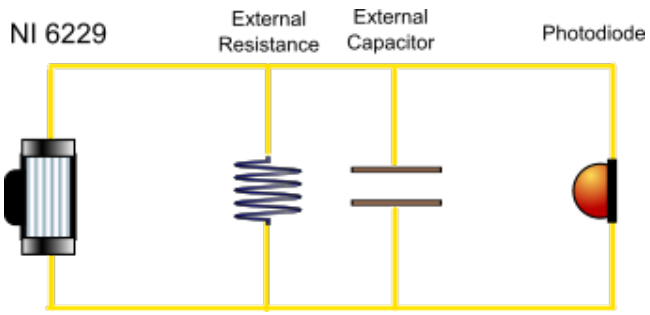

Figure 8.2 Electrical circuit for measuring input power.

During this measurement, the photodiode is attached to an up/down periodically moving arm. When the arm is at the lower position, the photodiode is in the beam path and measures the input Power, P_{in} (Figure 8.3). When the arm is at the upper position, beam propagation through the optical system is permitted and the transmitted Power, P_{tr}, is measured. To allow this measurement the receiver fiber has been curled around to position the exit at the same plane as the exit of transmitter coupler.

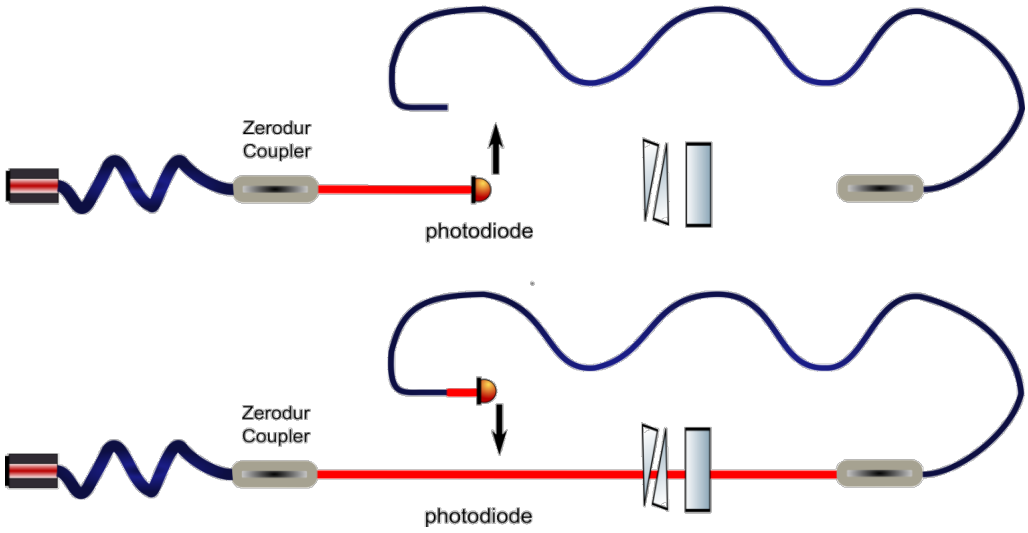

Figure 8.3 CE measurement. Up: First the input is measured. Down: The transmitted power is measured using the same photodiode.

In both measurements, the photodiode signals are proportional to the actual measured quantities:

$$S_1 = c\, P_{in}$$

$$S_2 = c\, P_{tr} \qquad (8.2)$$

where c denotes the responsivity of the photodiode. Combining (8.1)(8.2) the CE is then estimated by:

$$CE = \frac{S_{tr}}{S_{in}} \qquad (8.3)$$

Errors in our measurement may occur from various sources. Power fluctuations of the laser source affect the CE measurement accuracy. Another factor is the spatial homogeneity of the photodiode, i.e. the dependence of its signal on the actual sensor area that is illuminated. Both effects, temporal and spatial, are minimized by averaging, which along with measurement accuracy and noise set the error in our measurements. The experimental values of the total error of the measurement that have been observed are of the order of 1%.

Considering the effect of each element on the OBST breadboard has on the CE, we can estimate a lower value of the measured CE (Table 8.1).

Error	Value (%)	Total contribution (%)
Wedge reflectance (4 surfaces))	0.25 + 0.5/surface	1.0+2.0
Glass Plate reflectance	0.25+ 0.5/surface	0.5+1.0
Receiving lens reflectance	0.25+ 0.5/surface	0.5+ 1.0
Receiving fiber reflectance	0.25+ 0.5/ surface	0.5+ 1.0
Collimation error	1	1
Alignment error	0.5	0.5
Adhesion process	3	3
Total	-	7+5.0

Table 8.1 Error budget for CE.

- The reflectance of the elements are the nominal values by the manufacturers which is 0.25 for normal incidence. However, when taking into account that actual values may differ from nominal values and that the incident light is not normal, reflectance may increase significantly up to 0.5 per surface.
- The total contribution is calculated for a system with a wedge pair (4 surfaces) and one glass plate.
- Collimation and alignment errors originate from the precision of each procedure.
- The loss from the adhesion process has been derived through tests performed on the breadboard that has been assembled.

Expected values of CE, are in the range of 88-93% when taking into account the error budget.

In Figure 8.4 we can see some data collected from the integrated Zerodur breadboard and the calculated CE. As it is shown, the measured value of the CE is within the expected values, slightly above 89% with fluctuations less than SD<0,5%.

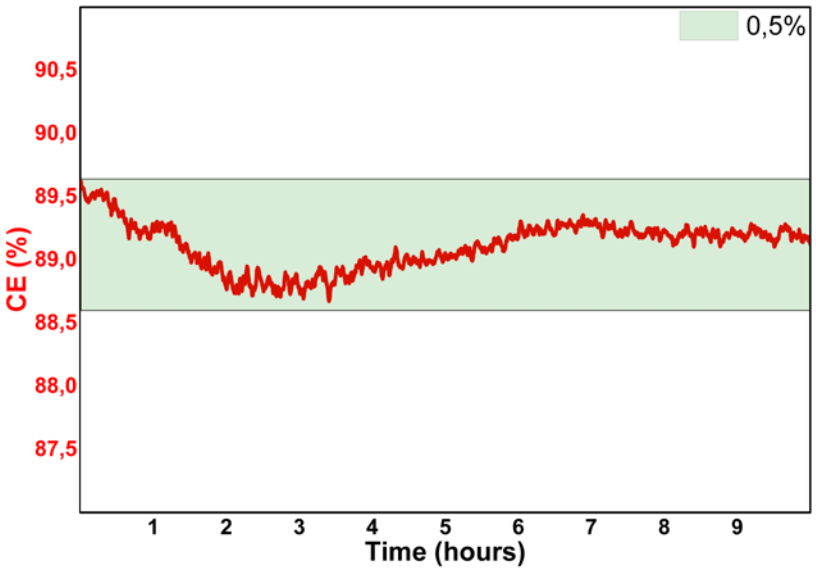

Figure 8.4 Measured CE along with the colored area being the standard deviation.

The next step is to test whether the breadboard can withstand temperature fluctuations without significant power losses.

8.2. Thermal stability

Temperature fluctuations occur in every space mission. Therefore, it is of paramount importance that the breadboard is able to perform at a range of temperatures. The thermal enclosure that will perform the thermal testing for the breadboard is shown in Figure 8.5. The thermal setup consists of a properly adapted fridge (AEG S71440TSW0) for cooling the system, a heating tape to heat it (Omega FGH052-080) and a fan to increase the circulation of air. For better control of the system we have also installed an insulating box, consisting of packaging foam, inside the fridge which provides smoother changes of temperature.

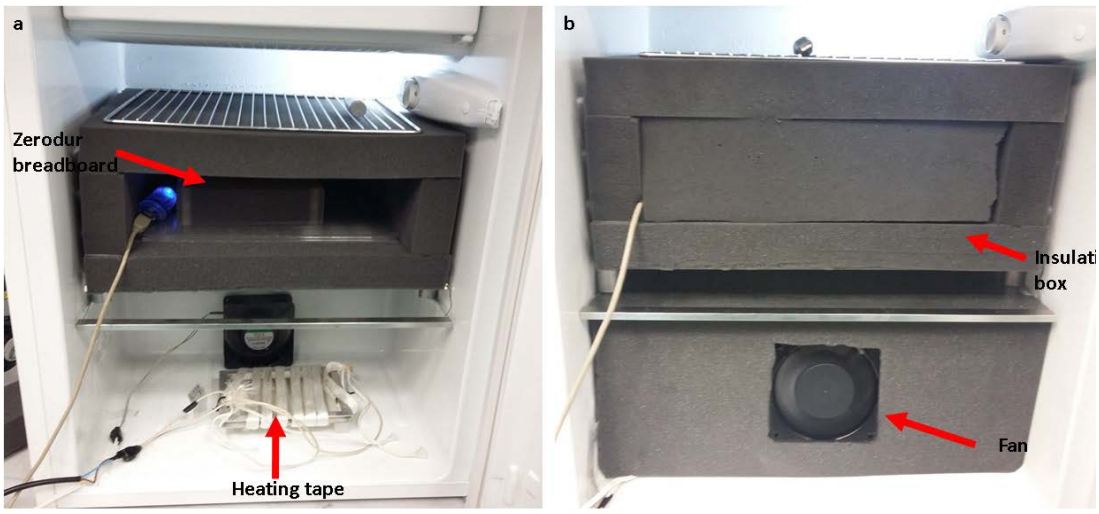

Figure 8.5 Thermal enclosure for testing thermal stability of OBST breadboard. In a, the insulating box has been opened to place the breadboard and a part of insulating foam has been removed to reveal the heating tape. In b, the insulating box is assembled.

The integrated breadboard is placed inside the insulating box and is subjected to thermal cycles. The experimental setup is capable of performing cycles between 10°C and 40°C during which the CE of the system is continuously monitored. The temperature is monitored with three thermistors which can measure temperatures with an accuracy of ±0.2°C. The temperature range of these thermistors is -40 to 125 °C and the response time is 0.4s. A thermistor is positioned on the zerodur breadboard, on a wedge holder and the last

one is measuring the temperature of the air above the breadboard.

Relative humidity is also monitored inside the insulating box to test any correlations with the CE. The humidity is monitored by a MicroLite usb sensor (Fourtec LITE5032P-RH-A). It can measure relative humidity from 5-95% with a 2% accuracy and resolution 0.05% the sampling rate is 1/s.

In Figure 8.6, the performance of the thermal enclosure can be seen. Several cycles have been performed in the desired temperature range.

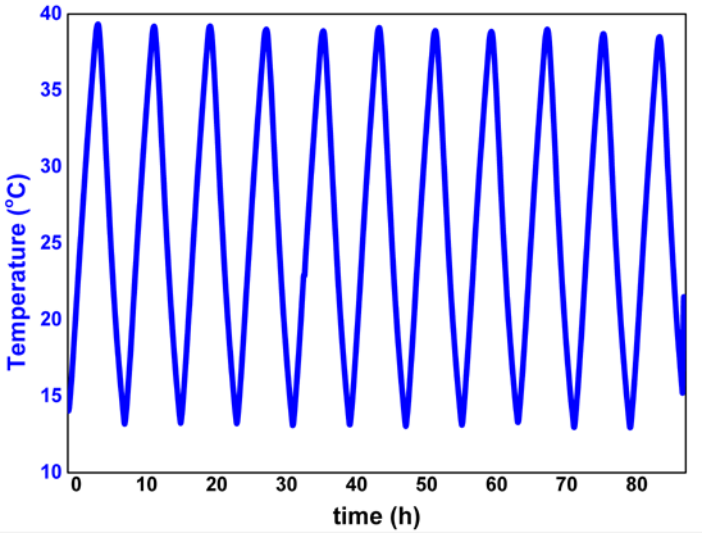

Figure 8.6 Raw data from thermal cycles of the interior of the insulating box.

The temperature stability of the testing environment has been also evaluated. Temperature data has been collected for 20 hours without any thermal cycling. For demonstrating stability over time, Allan Variance has been deducted from the experimental data and is presented in Figure 8.7. The stability of the system is better than $0.6mK/Hz^{1/2}$ while a common requirement is $10mK/Hz^{1/2}$.

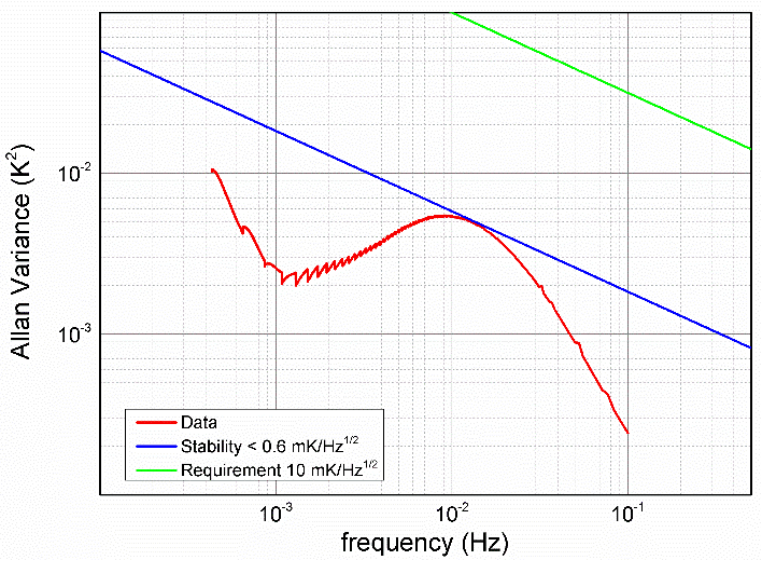

Figure 8.7 Allan Variance of the thermal testing environment.

8.3. Performance of Zerodur breadboard under thermal cycling tests

The integrated Zerodur breadboard with the optics has been subjected to thermal cycling while monitoring the CE. In Figure 8.8, temperature data along with the calculated CE are presented.

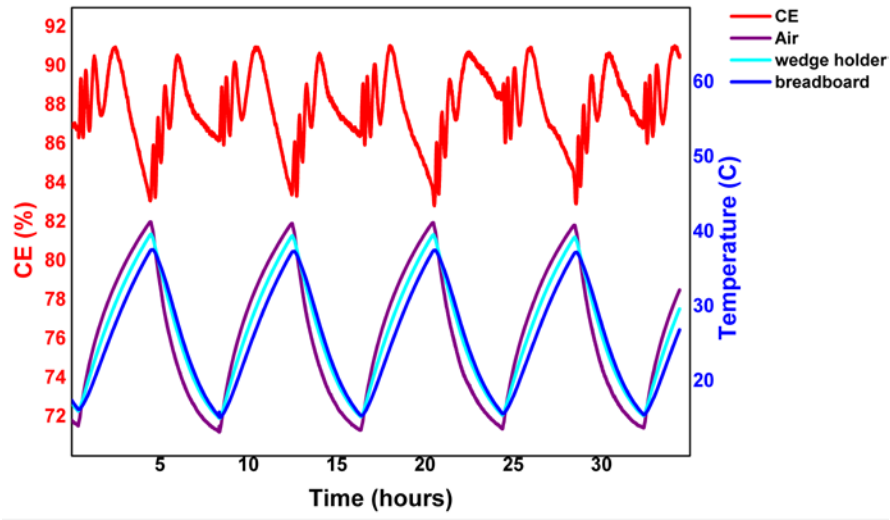

Figure 8.8 Measured CE during thermal cycles of the Zerodur breadboard.

As it is evident the fluctuations of the CE are quite high. The maximum value is 91% while the minimum is 83% which means that peak to peak fluctuations are of the order of 4% while the standard deviation of the CE is 2%.

Evidently, there are some fast oscillations during each thermal cycle, which indicate interference effects. The interference affects significantly the fluctuations of the CE since the interference clearly creates localized peaks and valleys of about 2%. The period of the high frequency peaks shown in Figure 8.8 is approximately 5^{o}C. Taking into account the CTE of the materials present on the breadboard, such oscillations can be produced by the zerodur breadboard or the air between the two ferrules. Independently of the underlying cause, a cavity is probably formed between the two ferrules of the fibers. Unfortunately, the ferrules are not angled cleaved because the supplier could not provide angle cleaved bare ferrule end on the fiber. Therefore, there is a possibility that these two flat surfaces are forming a cavity.

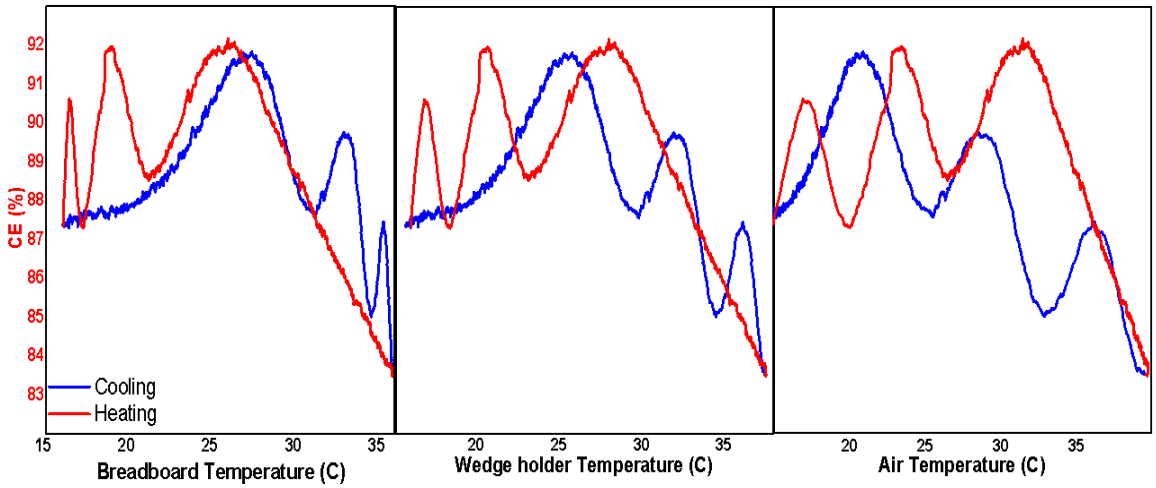

Figure 8.9 CE plotted against the temperature of breadboard, wedge holder and air. Heating phase and cooling are colored in red and blue respectively.

When the breadboard is submitted to thermal cycles, it expands and contracts, changing the length of the cavity and thus creating the fringes. This conclusion is supported by the plots of the CE versus the temperature of the breadboard (Figure 8.9). The correlation seems to be stronger between the CE and the breadboard where the overlap of the two central peaks is increased.

Nevertheless, the overall performance of the zerodur breadboard is encouraging. Although, the system can be improved, the resulting mean CE is high and fluctuations are not much worse than the expected performance of a prototype. If the side effects of the system are minimized and the true fluctuations of the system are measured, the actual performance of the breadboard will be revealed and safer conclusions could be deducted.

9. Conclusions

Novel beam steering techniques have been demonstrated and utilized to integrate a complete optical breadboard. The passive optical elements that were used, proved to be less sensitive to misalignments. Thus the tolerances of the manufactured Zerodur components could be relaxed decreasing the production cost and time. Furthermore, with the described alignment process the accuracy is increased significantly which leads to an increase in the CE.

Three different monolithic components were manufactured for the breadboard. Their design is simple and efficient permitting easy integration. Furthermore, the use of UV adhesive for the integration provides noticeable advantages. It is a much simpler and straightforward method, which reduces the demands on technologies for assembling an optical fiber breadboard.

The assembled optical breadboard performed above average. The measured coupling efficiency was within the expected values and if the simplicity of the designs is taken into consideration, the achieved CE is remarkable. The fluctuations during thermal cycles were slightly higher than those expected, probably due to some of the parts involved. Improving on the current prototype is the logical next step, which will exhibit the actual performance of the breadboard.

Concluding the whole project has demonstrated the validity of the proposed technique which reduces complexity but in the same time increases efficiency. All in all, this project produced significant and noticeable results that can stimulate even further research.

Bibliography

[1] H. Duncker, O. Hellmig, A. Wenzlawski, A. Grote, A. J. Rafipoor, M. Rafipoor, K. Sengstock, and P. Windpassinger, "Ultrastable, Zerodur-based optical benches for quantum gas experiments.," *Appl. Opt.*, vol. 53, no. 20, pp. 4468–74, 2014.

[2] C. J. Killow, E. D. Fitzsimons, M. Perreur-Lloyd, D. I. Robertson, H. Ward, and J. Bogenstahl, "Optical fiber couplers for precision spaceborne metrology," *Appl. Opt.*, vol. 55, no. 10, p. 2724, 2016.

[3] D. I. Robertson, E. D. Fitzsimons, C. J. Killow, M. Perreur-Lloyd, H. Ward, J. Bryant, a M. Cruise, G. Dixon, D. Hoyland, D. Smith, and J. Bogenstahl, "Construction and testing of the optical bench for LISA Pathfinder," *Class. Quantum Gravity*, vol. 30, no. 8, p. 85006, 2013.

[4] C. J. Killow, E. D. Fitzsimons, J. Hough, M. Perreur-Lloyd, D. I. Robertson, S. Rowan, and H. Ward, "Construction of rugged, ultrastable optical assemblies with optical component alignment at the few microradian level.," *Appl. Opt.*, vol. 52, no. 2, pp. 177–81, 2013.

[5] E. J. Elliffe, J. Bogenstahl, A. Deshpande, J. Hough, C. Killow, S. Reid, D. Robertson, S. Rowan, H. Ward, and G. Cagnoli, "Hydroxide-catalysis bonding for stable optical systems for space," *Class. Quantum Gravity*, vol. 22, no. 10, pp. S257–S267, 2005.

[6] F. Trager, *Handbook of lasers and Optics*, vol. 1. New York: Springer, 2007.

[7] F. J. Duarte, *Tunable Laser Optics*. Elsevier Science, 2003.

[8] S. Mukhopadhyay, "Misalignment considerations in a laser diode to monomode elliptic core fiber coupling via a hyperbolic microlens on the fiber tip : efficiency computation by the ABCD matrix," vol. 46, no. September 2007, pp. 1–5, 2015.

[9] E. Hecht, *Optics*. San Francisco: Pearson Education, 2002.

[10] J. M. Senior and M. Y. Jamro, *Optical Fiber Communications: Principles and Practice*. Essex: Pearson Education, 2009.

[11] S. R. Nagel, J. B. MacChesney, and K. L. Walker, “An Overview of the Modified Chemical Vapor Deposition (MCVD) Process and Performance,” *IEEE Trans. Microw. Theory Tech.*, vol. 30, no. 4, pp. 305–322, 1982.

[12] D. Gloge, “Weakly Guiding Fibers,” *Appl. Opt.*, vol. 10, no. 10, pp. 2252--2258, 1971.

[13] R. E. Wagner and W. J. Tomlinson, “Coupling efficiency of optics in single-mode fiber components.,” *Appl. Opt.*, vol. 21, no. 15, pp. 2671–2688, 1982.

[14] M. Bass, *Handbook of Optics. Volume II Design,Fabrication, and Testing; Sources and Detectors; Radiometry and Photometry.* 2010.

[15] G. Drougkakis, “Optical Breadboard Technologies for Complex Space Missions TN1 : Applications and Technology Report,” 2015.

[16] E. A. S. Bahaa and M. C. Teich, *Fundamentals of Photonics*. John Wiley & Sons, 1991.

[17] A. Macleod, *Thin film optical coatings*, vol. 129. New York: CRC Press of Taylor and Francis Group, 2010.

[18] Alluxa Engineering, “Durable , Front Surface Hard Optical Coatings for Replacing Laminated Soft Coatings.” 2012.

[19] F. Terms, “Equi-reflectance Contours of Double-layer Anti-reflection Coatings,” *Opt. Acta Int. J. Opt.*, vol. 11, no. 2, pp. 159–170, 1964.

[20] B. G. Yacobi, S. Martin, K. Davis, A. Hudson, and M. Hubert, “Adhesive bonding in microelectronics and photonics,” *J. Appl. Phys.*, vol. 91, no. 10 I, pp. 6227–6262, 2002.

[21] T. Gohlke, Martin Schuldt, K. Döringshoff, A. Peters, U. Johann, D. Weise, and C. Braxmaier, “Adhesive Bonding for Optical Metrology Systems in Space Applications.pdf,” *J. Phys. Conf. Ser.*, vol. 610, no. 1, 2015.

[22] S. Ressel, M. Gohlke, D. Rauen, T. Schuldt, W. Kronast, U. Mescheder, U. Johann, D. Weise, and C. Braxmaier, “Ultrastable assembly and integration technology for ground- and space-based optical systems,” *Opt. Soc. Am.*, vol. 49, no. 22, pp. 4296–4303, 2010.

[23] Norland Products Incorporated, “Optical Adhesives Datasheet.” 2016.

[24] 3M, “Transbond ™ Supreme LV datasheet.” 2008.

[25] Aremco, “Mounting adhesives & accessories Technical Bulletin A9.” .

[26] F. A. Hummel, “Thermal Expansion Properties of Some Synthetic Lithia Minerals,” *J. Am. Ceram. Soc.*, vol. 34, no. 8, pp. 235–239, 1951.

[27] Schott AG, “TIE-26 Homogeneity of optical glass,” 2004.

[28] Schott AG, “TIE-25: Striae in optical glass,” 2006.

[29] Schott AG, “Tie-43 Properties of Zerodur,” 2014.

[30] P. Hartmann, R. Jedamzik, S. Reichel, and B. Schreder, “Optical glass and glass ceramic historical aspects and recent developments: a Schott view,” *Appl. Opt.*, vol. 49, no. 16, p. D157, 2010.

[31] R. Rustum, D. K. Agrawal, and H. A. McKinstry, “Very low thermal expansion coefficient materials,” *Annu. Rev. Mater. Sci.*, vol. 19, pp. 59–81, 1989.

[32] V. Maier and G. Muller, “Mechanism of Oxide Nucleation in Lithium Aluminosilicate Glass-Ceramics,” *J. Am. Ceram. Soc.*, vol. 70, no. 8, pp. C176–C178, 1987.

[33] S. J. Schneider, J. R. Davis, G. M. Davidson, S. R. Lampman, M. S. Woods, and T. B. Zorc, *Ceramics and Glasses*. 1991.

[34] Schott AG, “TIE-35: Transmittance of optical glass,” 2005.

[35] Schott AG, *Zerodur ® – Zero Expansion Glass Ceramic catalogue*. 2011.

[36] Schott AG, “TIE-45: Zerodur adhesive bonding recommendations,” 2009.

[37] H. Kogelnik, “On the Propagation of Gaussian Beams of Light Through Lenslike Media Including those with a Loss or Gain Variation,” 1965.

[38] T. Li, H. Kogelnik, and T. Li, “Laser Beams and Resonators.pdf,” *Appl. Opt.*, vol. 54, no. 10, 1966.

[39] M. Bass, E. W. Van Stryland, D. R. Williams, and W. L. Wolfe, *Handbook of Optics Vol IV*. New York: McGraw-Hill Companies, 2001.